Structural and lithological control on fluid circulation, dilation andore mineralization(Rio Albano mineIsland of Elba, Italy)

Mazzarini F.[1], Musumeci G.[1,2], Viola G.[3], Garofalo P.S.[3], Mattila J.,[4,5]*

1-Istituto Nazionale di Geofisica e Vulcanologia, Pisa,Italy
2-Dipartimento di Scienze della Terra, Universityof Pisa, Italy
3- Dipartimento di Scienze Biologiche, Geologiche e Ambientali, University of Bologna, Italy
4- Geological Survey of Finland, Espoo, Finland
5- Currently at Rock Mechanic Consulting Finland Oy, Vantaa, Finland

Abstract

We present the results of geological and structural investigation documenting the interaction between hydrothermal fluids and host rock leading to a vein-type ore mineralization at shallow crustal depths (< 7 km) in the mining district of the eastern Island of Elba (Italy). Sulfide- and iron-rich veins and breccia in addition to minor massive iron-ore bodies form the mineralized system.Structural mapping and analysis of vein systems, fractures, faults and associated fault rocks as well as fracture opening modesshow thatthe main factors controlling the formation and distribution of the mineralization are lithology, deformation style and deformation intensity.Their interplay led to a positive feedback between the evolution of pore pressurethrough time, strain localization and the resulting mineralization. Inversion of fault and vein data defines anE-W extensionalstress field at the time of faulting,which favored fluid ingress and pervasive flow within the porous host sandstone, interstitial sulfide precipitation and reduction of the primary bulk porosity. Subsequently, cyclic channelized fluid flow duringrepeated fluid ingressescaused extensive veining and numerous episodes of breccia formation.

Keywords: hydrothermalism, upper crust, faulting, fluids, structural analysis, Island of Elba, Northern Apennines

* Corresponding author: Francesco Mazzarini, Istituto Nazionale di Geofisica e Vulcanologia, Via Santa Maria 32, 56 126, Pisa, Italy, phone +39 0508311956, email: francesco.mazzarini@ingv.it

1. Introduction

Crustal fluids are commonly involved in metamorphic, magmatic, hydrothermal, and ore body formation processes (e.g., Oliver 1996). In fact, mineralizations (i.e. mineral veins an ore bodies), alteration haloes and hydrothermal breccias attest to fluid circulation within the crust exploiting actual fracture networks or forming new fractures.

In this contribution the term fractures is used according to the definition in National Research Council, (1996): "*Fractures are mechanical breaks in rocks involving discontinuities in displacement across surfaces or narrow zones. Fracture is a term used for all types of generic discontinuities. ……. However, different kinds of fractures exist, with different geometries, mechanical effects, and flow properties. Based on the nature of the displacement discontinuity, commonly encountered fractures can be classified into three geologically based major groups: (1) dilating fractures/joints, (2) shearing fractures/faults, and (3) closing fractures/pressure solution surfaces*".

We use the term fracture consistently with these definitions to indicate a break in a rock where the orthogonal opening is predominant; on the contrary, if clear lateral displacement by shearing is observed, then we adopt the term fault.

The generally acknowledged driving mechanisms for fracture opening include tectonic stresses exceeding the strength of the rock, changes in pore-fluid pressure leading to hydrofracturing and the role of the overburden. An extensional fracture opens in a direction parallel to the maximum tensile (minimum compressive) principal stress. There are two main types of extension fracture: i) tension fractures, which form when the stress perpendicular to the fracture is negative, and ii) hydrofractures, which open when the fluid pressure is sufficient to counteract the stress acting perpendicular to the fracture plane. While tension fractures form at shallow depth, hydrofractures may form at any depth when $\sigma_3 - P \geq T$, where σ_3 is the minimum stress, P the fluid pressure and T is the tensile strength of the rock

(e.g., Gudmundsson, 2011). Planar discontinuities in the host rock, stiffness changes between contiguous layers, and stress barriers, where the local stress field is unfavorable to hydrofracture propagation, may all cause the arrest of hydrofractures (see Philipp et al., 2013 for a review).

Several studies demonstrate that hydraulic fracturing is a very common and important fluid-assisted brittle deformation type (e.g., Hubbert and Willis 1957; Ramsay 1980; Cox 1995; Philipp et al., 2013).

Linking fluid pressure variations and mineral precipitation within fractures is a not straightforward task.In sedimentary rocks, veining may occur by interaction of fluids with the surface of the fracture's walls forming quartz cement during burial and later exhumation histories (e.g. Lander and Laubach, 2015; Becker et al., 2010).In passive margin deep basinal settings, fractures can remain hydraulically active over geologically long times (several tens of million years; Becker et al., 2010) with low opening rates (Lander and Laubach, 2015; Becker et al., 2010). On the other hand, hydrofractures and metamorphic veins may develop rapidly (less than 200 yr) relative to rates of metamorphic processes (e.g, Nishiyama, 1989).

Fluids flowing along fractures can be of internal origin or may derive form external sources. Fluids descending through the rock columnsuggest fracture opening driven by external stresses such as those due to tectonism or decompression rather than an increase of fluid pressure. (e.g. Hooker et al., 2015), whereas fluids from sources at depth invoke fluid pressurizationand hydrofracturing (e.g. Mazzarini et al., 2011; 2014).

Fractures can thus become mineralized when fluid pressure dropsand breccia may form when local, transiently high pore pressure values are attained (e.g., Bons, 2001, Cox et al. 2001).

Brecciasare common in shallow, fluid-saturated, upper crustal deformationzones, andareamong the most widely distributed fault rocks in hydrothermal ore deposits(e.g., Sillitoe, 1985; Jébrak, 1997).Breccia formation may result from the combined effects of

tectonic, chemical and hydraulic processes (Jébrak, 1997; Clark and James, 2003; Cox, 2010; Sibson, 1986). Thus,constraining the processes of breccia formation is relevant to the understanding of the mineralization environment, faulting in general and hydrothermal systems (e.g. Jébrak, 1997; Cox and Munroe, 2016).

Brittle failureleads todilation and comminution of therock as part of a cataclastic flow process;when fluid-mediated,faulting may induce fluid-rock interaction and lead topartial dissolution of the host rock and deposition of minerals that may be localized or disseminatedin the deforming host rock volume depending on the fluid circulation/diffusionpaths and the lithology porosity (channelized vs.pervasive systems; e.g. Oliver, 1996).

Here we present asignificant case in the mining district in the eastern Elba of Island (northern Apennines, Italy), where different types of hydrothermal deposits within a lithologically homogeneous rock volume attest to the development and interplay in space and through time of both pervasive and channelized fluid circulation. We show that both lithologyand deformation path controlled the formation and distribution of hydrothermal brecciaand mineralized veins and steered the feedback between mineralization, fluidand deformation.

3. Methods used for the structural analysis of the hydrothermal system

In order to study the relationships between deformation and fluid circulation in Elban hydrothermal vein systems and ore deposits we applied several methods to single out the possible mechanism of hydrothermal breccia formation and to constrain the state of stress and the fluid pressure at the time of mineralization. Detailedfield observation of remarkable exposures (i.e., vein thickness, vein distribution, breccia grain size and fault kinematics; the reader is referred to Appendix A for the extensive description of the methods) invariably served as starting point of our study.

3.1 Vein thickness distribution analysis

Vein thickness distribution in a rock mass can be used to infer the mechanism responsible for vein growth, hence fracturing (e.g. Clark et al., 1995; Roberts et al., 1999; Hooker et al., 2014).The distribution of vein thickness in a given rock volume (see Appendix A1) can be described by power-law or negative exponential relationships (e.g. Johnston and McCaffrey, 1996; Gillespie et al., 1999; Loriga, 1999; Roberts et al., 1999; Hooker et al., 2014; Mazzarini et al., 2014).

3.2 Particle Size Distribution (PSD) analysis of hydrothermal breccia

Hydrothermal deposits commonly incorporate breccias resulting from numerous possible mechanisms of brecciation, which reflect the interplay of various physical and chemical mechanisms such as tectonic comminution by cataclastic flow, wear abrasion, fluid-assisted brecciation, volume dilation and collapse (i.e. Jébrak, 1997 and references therein). Breccias are essentially composed by angular and heterometric fragments embedded within variable amounts of finer matrix (e.g., Sillitoe, 1985). The analysis of the size distribution of the fragments of the brecciated rocks (see Appendix A2) has been long applied to fault rocks (Scholtz, 1987; Sammis et al., 1987; Sammis and Biegel, 1989) and also widely used in empirical studies in the mining sciences to establish the processes responsible for the comminution of the host rock (e.g. Blenkinsop, 1991). Empirical data indicate that the actual fragment size distribution is steered by the activated fragmentation process, initial size distribution, number of fracturing events, energy input, finite strain, and the confining pressure (e.g. Blenkinsop, 1991).

3.3 Mohr circle, stress state and fluid pressure analysis

According to Jolly and Sanderson (1997) the analysis of vein distribution might provide an estimate of the stress state at the time of veining as expressed by a representative Mohr circle and fluid pressureestimate (see Appendix A3). The stress ratio Φ (where $\Phi = [(\sigma_2 - \sigma_3)/(\sigma_1 -$

σ_3))] and the driving stress ratio *R'* (where R' = [(P_f–σ_3/(σ_1 - σ_3)] are defined in terms of the principal stresses (σ_1, σ_2, σ_3) and fluid pressure P_f (Jolly and Sanderson, 1997; see Appendix A3).The ratio of fluid pressure to the vertical stress (lithostatic load for an extensional stress field) is the pore fluid factor $\lambda_v = P_f/\sigma_v$ (e.g. Sibson, 2000) where P_f is the fluid pressure and σ_v is the vertical lithostatic stress.In the case of an extensional stress field, $\sigma_v = \sigma_1$; if the differential stress is constrained, it is then possible to infer the values of the principal stresses by applying the empirical relationships of MacGarr (1980) for shallow crustal depths (< 7 km) or by using the theoretical approach of Lisle and Srivastava (2004; seeAppendix A3).

3.4 Dilation and slip tendency analysis

Slip tendency (T_s) and the dilation tendency (T_d) analysis (see Appendix 4) are used to investigate the propensity to slip and/or dilate of a faultwithin a given stress field (e.g., Collettini and Trippetta, 2007; Viola et al., 2012; Ferrill et al., 2017).

3. Geological setting

3.1 Island of Elba

The Islandof Elba (Figure 1a)exposes a tectonostratigraphic sequence formed by metamorphic and non-metamorphic units derived from both continental (the Tuscan Nappe) and oceanic (the Ligurian Unit) domains stacked toward the northeast during the Oligocene–Miocene Apenninic orogeny (Massa et al., 2017 and references therein).These tectonic unitsarefundamentally organizedinto two major thrust complexes (e.g. Musumeci and Vaselli, 2012; Massa et al. 2017), with an Upper Complexformed by an imbricate fan of three thrust sheets madeup of sedimentary and low-grade metamorphicrocks belonging to Ligurian units and TuscanNappe and a Lower Complex consisting of two metamorphic units, namely theCalamita Unit overlain by the OrtanoUnit (Figure 1a). According to several reconstructions (e.g., Keller and Coward, 1996; Pertusatiet al., 1993;Musumeci et al., 2015;

Massa et al., 2017), thetectonic evolution ofthe nappe stack exposed in the easternmost Island of Elba can be summarizedin three stages:(i) Oligocene early folding and nappe stackingunder very low metamorphic grade (i.e., anchizone) in the upper complex andlow metamorphic grade (i.e., epizone) in thelower complex;(ii) middle Miocene extension of the stack upper portion due to the gravitational collapse of the over-thickened orogenic wedge (Massa et al., 2017) followed by (iii) middle-late Miocene out of sequence folding and thrusting that deeply reshaped the nappe stack (Musumeci and Vaselli, 2012; Papeschi et al., 2017; Viola et al., 2018). Two large monzogranitic intrusions(Monte Capanne and Porto Azzurro plutons) accompanied by swarms of leucogranitic sills emplaced between ca. 8 to 5.9 Ma (Dini et al., 2002). K-Ar radiometric dating of synkinematic illite in fault gouges from the main tectonic contacts deforming the nappe stack argue for a complex tectonic evolution wherein shortening pulses seem to have continued to the early Pliocene, interrupting the background extension that started in the Miocene (e.g. Viola et al., 2018).

Thenappe stack exposed on eastern Elba forms a large, west dipping monoclinal structure that resulted from middle Miocene folding and thrusting within the growing orogenic wedge (Massa et al., 2017; Viola et al., 2018). Within this monocline, west-dipping thrusts (i.e. the thrust separating the Lower and Upper Complexes andthe thrust sheets within the Upper Complex) and mesoscale folds generally strike from N–S to NNW–SSE (Figure 1a).

In the study area (Rio Albano mining district; Figures 1b, c), the Upper Complex consists of the Rio Marina Unit, which is tectonically overlain by the Tuscan Nappe along a thrust fault in the west and a syn nappe-stacking extensional fault in the east (Figure 1a). The Rio Marina Unit consists of late Carboniferous-early Permian phyllite and metasandstone (Rio Marina Formation), followed upward by middle-upper Triassic conglomerate, phyllite, sandstone and white-green quartzite and quartzitic breccia (Verruca Formation and Quarziti del Monte Serra Formation; Rau & Tongiorgi, 1974) belonging to the Verrucano siliciclastic deposits

(Verrucano Group of Aldinucci et al., 2008).

3.2. Ore deposits on Elba Island and in the Rio Albano area

With seven distinct ore deposits exploited from pre-Etruscan times to 1981 (i.e., for almost three millennia), the Island of Elba is the historically and economically most important Fe district of Italy (Tanelli et al., 2001 and refs. therein).

The economic relevance of this district is also highlighted by its documented Fe ore tonnage, which, for example, for the relatively short 1900-1975 period is reported to 50-55 Mt (Zitzmann, 1977). The Topinetti section studied here is located between the two northernmost deposits of the Elba district, i.e. Vigneria-Rio Marina in the south and Rio Albano in the north (Figure1b).The studied outcrop is located c. 500 m south of the Rio Albano deposits. Mine reports from Rio Albano (Anonymous, 1943; Calanchi et al., 1976; Gilliéron, 1959) show that lens-shaped ore bodies having thicknesses up to 20 m were bound by east-dipping faults, and hosted a systematic distribution of ore minerals. Limonite, magnetite, and hematite occurred in the shallowest section of the lenses, partly within the faults and partly within the immediate host rock. Hematite (specularite variety) was the most abundant mineral at the core of the lenses while pyrite was more abundant at depth. Quartz and calcite are reported as the main gangue minerals. The host rock is a sequence of Permo-Triassicquartzite, conglomerate, shale, and sandstone of the Verrucano Group that istectonically overlain by brecciated dolomitic limestone of Raetian age (CalcareCavernoso) and Liassiclimestones.

The age of Fe-ore formation at Rio Albano is partly constrainedby the age of the hematite-adularia ore in the neighboring Rio Marina deposit, where U/Th/He hematite dating and K/Ar adularia dating yielded ages of 6.4 ± 0.4 Ma and 5.3 ± 0.2 Ma, respectively(Lippolt et al., 1995).

A more recent study focusing on all Fe-deposits from Elba (Dünkel, 2002)shows that only one generation of magnetite formed at Rio Albano followed by two distinct generations of

hematite (including the platy specularite variety). This was determined as a peculiar paragenetic characteristic of Rio Albano and Rio Marina that is not found in other Fe-deposits of the island.

There is no accepted genetic model for the Fe-mine district of Elba, and for Rio Albano in particular. Earlystudies(e.g., Lotti, 1886; see also: Lotti, 1910), which can be considered among the earliest field documentation of metasomatic processes in ore-forming environments, interpreted the Fe deposits as epigenetic and magmatic-hydrothermal in origin. Later investigations(Bodechtel, 1965; Deschamps et al., 1983a; Deschamps et al., 1983b; Dünkel, 2002, and ref. therein; Tanelli et al., 2001)suggested instead genesis from a thermo-metamorphic event that involved the inherently Fe-rich, Palaeozoic-Triassic sedimentary source rock.

4. The Topinetti section: geology and mineralization

4.1 Geological setting

In the Rio Albano mining district, we studied a well-exposedhydrothermal system and its associated ore deposits between Rio Albano in the south and CalaSeregola in the north along a c. 300 m long coastal section (Figure 2). This section, hereinafter named the Topinetti section,has an actual maximum thickness of c. 200 m (Figure 2) and is characterized by whitish,plane parallel-laminated and cross-stratified quartziticsandstone and arkose with centimeter-thick layers of pebbly conglomerate andmetric layers of green-purple pelite(Anageniti minute Member of Verruca Formation; Rau and Tongiorgi, 1974) passing upward to massive to coarsely parallel-stratified white-grey quartzite and quartzitic breccia (Quarziti bianche Member of the Quarziti Formation of Rau and Tongiorgi, 1974).Sandstone and quartzite are both characterized by centimetricto decimetric beds dipping gently to moderately to NE, N and NW and are folded by trains of mesoscopic and gently northeast

plunging folds (Figure 3a).

The section can besubdivided into three sectors on the basis of lithology. A southern sector (sector 1 in Figure 2a) is characterized by arkose, quartzite, micro conglomerate and green-purple pelite. The central sector (2 in Figure 2a) is characterized by the widespread alteration of the same lithological sequence of sector 1 with sulfide-rich domains (Figure 2b) mostly localized at the contact between sandstone,quartzite and quartziticbreccia. The northernmost sector (3 in Figure 2a) consists of quartzite and quartzitic breccia and contains the main ore bodies of Topinetti, which progressively taper out toward the north due to their lensoidal shape.

N-S, E-W and NE-SW trending systems of subverticaltensile and hybrid fractures cut across the mineralized quartzite and quartzitic breccia (Figure3b). The associated vein systems mimic the fracture attitude, but, additionally,form also gentlydipping sets (Figure 3c). High- to low- angle N-S to NE-SW trending normal faults and strike slip to oblique normal E-W trending faults cut the quartzite as well as the hydrothermal breccia and the ore bodies (Figure3d).Using the massive ore bodies as a marker, the maximum observed net slip of the normal faults is constrainedto a maximum of c. 20 m. However, the offset of most of the normal faults is less than a few meters. The E-W faults cut across and offset generally by< 10 m the N-S and NE-SW faults. Fault geometric and kinematic analysis (Figure 3d) indicates an overall E-W extension with $\sigma_v = \sigma_1$.

4.2 Topinetti mineralization

The mainmineralizationishosted in the white-grey quartziteand quartzitic breccia and is made of hematite-dominated ore sub-types. Itconsists of:(i) intergranular pyrite grains, (ii) vein systems, (iii) hydrothermal breccia layers, and (iv) massive ore bodies. In the following, for the sake of clarity, the quartzite and quartzitic breccia will be defined as quartzite.

4.2.1Intergranular pyrite

Fine to medium-grained euhedral pyrite grains are disseminated within the porous quartzite (Figure 4a). These intergranular crystalsare found in the entire studyarea, withtheir abundance locally increasing to formcentimetric pyrite-rich pockets.

In thin section, pyrite is generally observed as single grains or polycrystalline aggregates (Figure 4b) thatinvariably overgrowthe rock fabric with the partial or almost complete replacement of quartz. These grains forms at triple junctions of quartz grains in the quartzite (Figure 4b) leading to an overall host rock porosity reduction.

Porosity in quartzite is generally low (0-2%; Manger, 1963; Kim et al., 2014; Poelchau et al., 2014; Durr and Sauer, 2015).In order to obtain an estimate of porosity reduction in the studied samples we analyzed the sample shown in Figure 4b by means of image analysis with the ImageJ software package (https://imagej.nih.gov/ij/).

The thin section area in pixel unit is 19961856 px and the area filled by pyrite is 32491 px. Assuming an original porosity ≤ 1% (e.g., Poelchau et al., 2014; Durr and Sauer, 2015),the area filled by pyrite expresses an at least 16%reduction of the primary porosity.

4.2.2 Vein systems

The mineralized vein system consists of sulfide- and hematite-bearing veins crosscutting at high angle the host rock bedding (Figures 4c, 4e). Sulfide-bearing veins have an average thickness of ~16 mm whereas hematite-bearing veinsare on average ~40 mm thick (Table 1).Veins dip steeply to moderately, with about 60% of them with a dominant NNE-SSW trend dipping > 70°, and the E-W and NW-SE representing only minor trends (Figure 5, left panels).

Sulfide and hematite-bearing veins mainly infillextensional fractures although, locally, they are also associated with hybrid fractures and display evidence of coexisting orthogonal dilation and shearing as testified by their local “en echelon” arrangement and asymmetric forking at vein termination.

At the micro-scale, sulfide veins crosscut all previous textures of the host rock and contain up to ~500 μm euhedral pyrite crystals (Figure 4d). Euhedral pyrite grains up to ~40 μmin sizeare also found in the matrix of the quartzitic breccia.

Hematite veins consist of a fine, dark hematite groundmass containingvery fine angular clasts of the host rocks (quartzite and quartz and pyrite rich breccia; Figure 4f). Veins formed by a dark hematite-rich matrix with clasts of host rocks alsooccur with an average thickness of ~64 mm (Table 1). They havevariable orientationandexhibit evidence of brecciation of the host rock (Figures 4g and 4h). The micro-fabric of these veins will be described in the hydrothermal breccia section (see below Breccia II).

The depth of vein formation and the fluid composition can generallybe derived by fluid inclusion and isotopic analysis (Becker et al., 2010; Hooker et al., 2015; Mazzarini et al., 2010). In Topinetti, however, we do not have such information and further geochemical and geochronological studies are necessary to constrain the P-T conditions at the timing of vein and breccia formation. This limitation notwithstanding, we can attempt to derive the depth at which veins formed based on the following geologic constraints:

1) The precipitation temperature of hematite in the Rio Albano-Rio Marina ore district is in the 180-200 °C range (Dünkel, 2002).

2)The current geothermal gradient in the still active geothermal fields of southern Tuscany and northern Latium varies between 40and 50 °C km^{-1} in the external portion of the geothermal fieldsand increases up to >100 °C km^{-1}in the central portion (Cataldi et al., 1978; Della Vedova et al., 2008).

3) Eastern Elba represents a late Miocene fossil geothermal field (Bertini et al., 2006; Dini et al., 2008) and a geothermal gradient similar to that occurring in the external portion of the active geothermal fields (i.e. 40-50 °C km^{-1}) can be reasonably assumed.

By using the temperature gradient of the still active external geothermal areas and the

estimated temperature range for hematite precipitation (Dünkel, 2002),the depth of veinformation in Topinetti can be constrained to the 3 – 5 kmdepth range. This estimate compares well with the estimated 3 - 5 km depth range for the low temperature, upper crustal, hydrothermal calcite-rich vein systems hosted in the Oligocene sandstones of the Macigno Formation in southern Tuscany to the east of the Island of Elba (Mazzarini et al., 2010; Mazzarini et al., 2014).

4.2.3 Hydrothermal breccia layers

In the central (sector 2 in Figure 2a) and northern (sector 3 in Figure 2a)sectors the host quartziteis characterized by the presence of volumetrically diffuse meter- to decameter thick breccia layers that, based on their texture and composition,are distinguished herein between (i) Breccia I and (ii) Breccia II (Figures6a, 6b).

Breccia I forms metric layers(from 1 to 5 m thick) of clast-supported breccia with clasts of quartzite embedded in a pyrite, chlorite, hematite and quartz-rich matrix.Clastsarecentimetric to decametric in size (up to 24 cm). The matrix fills intergranular voids andmayrepresentup to 10% of the total rock volume (Figure 6a). Most breccias formed within quartzite layers andtheir total volume can be estimated to ~$3.6x10^3$ m^3 (corresponding to outcrop dimensions of ~20 m along the NNE-SSW direction and ~60 m along the WNW-ESE direction with an average thickness of ~3 m). At thin section scale, quartz occurs as (i) coarse-grained anhedral,plastically strained grains (undulose extinction) and (ii) fine-grained euhedral grains (Figure 7a), the latter associated with pyrite (Figure 7a). Notably, two generations of pyrite are also present, with one euhedral coarse grained and another fine grained and subhedral to anhedral(Figure 7b). The second generation overgrows the first or infills late crosscutting veins.

Breccia II (Figure 6b) is formed by decimetric to metric (3-4 m),matrix-supported chaoticbreccia containing clasts of quartzite and Breccia I as well as cm-size pyrite grains

dispersed within a very fine-grained hematite-rich matrix that volumetrically can represent up to 70% of the rock.The main body of Breccia II consists of an exposed volume of ~$2x10^4$ m^3 (corresponding to outcrop dimensions of ~40 m along the NNE-SSW direction and ~150 m along the WNW-ESE direction for an average thickness of ~4 m) that rests paraconformably on quartzite and micro conglomerate, although locally it injectsinto the quartzite and Breccia Iwith clear evidence of hydrofracturing (Figure 4g).At thin section scale, the matrix in Breccia II is composed of very fine, newly formed euhedral hydrothermal quartz associatedwith hematite (Figure 7c). Hematite in the matrix is made of an aggregate of elongated euhedral hematite platelets forming boxwork textures (Figure 7d).

4.2.4 Massive ore bodies

Metric, stratabound massive ore bodieswithin theVerrucaFormation quartzite(Figures 6c and 6d) consist of hematite and minor magnetite,although no magnetic effects close to the ore bodies were observed. They rest conformably over the large volumes of Breccia II. The cumulative thickness of individual ores is up to 10 m in sector 3 (Figure 2a). No veins cut the ore bodies suggesting that they may represent the last mineralization episode of the system.

4.2.5 Relationships between brittle deformation and the hydrothermal system

Field observations suggest complex relationships between brittle deformation (i.e. fractures and faults) and the evolution of the hydrothermal system. Veins and fractures share similar planar attitudes although veins also occur as moderately to gentlyN to NW dipping (Figure 3c). N-S, NNE-SSW and NNW-SSE fracture sets are coherent with Riedel fracture systems associated withN-S to NNE-SSW high and low angle normal faults (Figure 8a). Sulfide- and hematite-vein distributions are characterized by aplanar attitude distribution similar to that of faults (Figures 8b and 8c). Breccia II and faultsshare very similar orientations (Figure 8d).Results from inversion of fault- (Figure 3d) and sulfide, hematite and Breccia II veins

(Figure 5 left panels and Table 4)are consistent withoverall E-W extension during faulting and vein emplacement.

Iron rich fluids precipitatinghematite veins and the matrix of Breccia II were syn-kinematic to the activity of the studied faults as shown by pure hematite and hematite-rich breccia decorating the fault planes and forminghematite growths and slikenlines (Figures 6f, 8e, 8f and 8g). However, hematite and Breccia II veins cutting the fault planes have also been observed, which suggests post-kinematic relationships with faulting. These observations attest, in turn, to an active role of faulting in steering fluid ingress and circulation in the quartzite host rock. On the other hand, also faults cutting across hydrothermal veins, breccia and ore bodies (Figure 6d, 6e) and veins emplacing within fault planes (Figure 8h) are observed.

In summary, at Topinetti hydrothermal veins and breccias show pre-, syn- to post-kinematic relationships with faulting suggesting that fluids and faults interacted in a complex and possibly cyclic fashion.

5. Size Distribution analysis

5.1 Vein thickness size distribution analysis

Vein thickness has been measured along transects placed at least 50 m apart in order to avoid oversampling (i.e. measuring repeatedly the thickness of the same veins). Vein thickness (w) was measured normal to the vein walls and we recorded for each vein the largest exposed thickness. The choice of the fitting distribution (see Appendix A1) was done aiming at: 1) the lowest difference between the theoreticaland the observed maximum thickness value, and 2) the largest size range with the highest correlation coefficient.

Sulfide vein thickness exhibits a power law distribution with exponent 1.191in the 5 – 130 mm size range (Table 2).The difference between the theoretical maximum thickness (i.e. the

maximum thickness derived from the distribution) and the observed maximum thickness for sulfide veins is 0.8%.

Hematite veins have a negative exponential distribution in the 0.1 – 140 mm size range (Table 2) and the difference between the theoretical maximum thickness and the observed maximum thickness for hematite veins is 1.4%.

Breccia II veins havea negative exponential distribution (Table 2) with the difference between the theoretical maximum thickness and the observed maximum thickness of 0.1%. Breccia II veins display also a power law distribution with exponent 0.834 in the 9 – 280 mm size range and coefficient of correlation higher than that of the exponential distribution (Table 2).In this case the difference between the theoretical maximum thickness and the observed maximum thickness for breccia II veins is as high as 76.6%.

Sulfide veins exhibit a fractal thickness distribution (Figure 9a) with a high fractal exponent (1.191) indicating predominance of thin fractures.Power-law exponent values > 0.8 have been reported for fractures and veins in metamorphic and hydrothermal systems (Andre´-Mayer and Sausse, 2007; Hooker et al., 2014). Hematite and Breccia II veins exhibit a negative exponential thickness distribution (Figure 9b,c).

5.2 Breccia II PSD analysis

For the Breccia II particle size distribution (PSD) analysis we usedthe following strategy:

i) Two pictures (samples 407 and 398) of the same outcrop were taken in order to properly document and represent the representative texture of Breccia II and to reduce the noise due to shadows and irregular surfaces (Figures10a, 10b);

ii) In the same outcrop we collected a sample for microscopic investigations and two photos of the thin section produced from that sample at different scales (samples 39 and 40)were used for the analysis (Figure 10c, 10d);

iii) In the analyzed images,fragmentsintersected by the edge of the imagewere discarded to

reduce border effects.

The particle size distribution of brecciasis often characterized by exhibiting a well-defined trade-off length in log-log diagrams that separatestwo distributions with different slopes for grains with size smaller and higher than the trade-off length(e.g., Keulen et al., 2007).

During comminution very small particles formin both experiments and natural fault rocks (Keulen et al., 2007 and references within). Kendall (1978) demonstrated that there should exist a limit in size (grinding limit) under which particles cannot be further comminuted; for example, the grinding limit is 0.9 μm for quartz and 2.2 μm for calcite and a trade-off length for fragmented rocks may stem from their typical grinding limit (Keulen et al., 2007 and references within).

A trade-off lengthmay, however,also derive from a sampling bias, i.e. from truncation and censoring effects (Bonnett et al., 2001; and Appendix A2). Truncation affects almost all the analyses and in our case reflects the resolution of the microscope and the camera used for the study. The definition of the fractal exponent over a range larger than one order of lengths reduces theeffects of truncation. The ratio between the maximum particle's diameter observed (D_{max}) and the dimension of the observation window (L_o) allows controlling possible censoring effects. Large ratio values ($\geq$1) may indicate that important censoring effects probably occurred, while low (< 1) ratio values indicate that censoring is not relevant in the analysis.

Sample images (Figure 10) were processed to produce binary b/w images for particle geometry measurements.We determined the Feret diameter (Walton, 1948) for each particle by using the tools in the ImageJ software package (https://imagej.nih.gov/ij/).

Fractal analysis of the Breccia II PSD data (Table 3 and Figure 11) shows the occurrence of a trade-off length for micro (1 mm) and meso (15 mm) scale samples.These trade–off values are higher than the grinding limit for the fault rocks (e.g. Keulen et al., 2007). Truncation

effects are not considered in the trade-off length definition because for $l<r_k$ the range of lengths used for all samples is higher than one order (Table 3). Also, censoring is not considered because all analyzed samples show low (< 0.3) "maximum particle diameter to observation window's size" ratio(Table 3).

Our analysed samples were plotted in the D_r-D_s diagram of Jébrak (1997) according to the computed values reported in Table 3. Mesoscale samples (398 and 407) fall within the "corrosive wear" field, whereas microscale samples (samples 39 and 40) fall into the "volume expansion" field (Figure 12).

6. Fluid pressure and Mohr circle of the vein systems

The analysis of vein systems may provide information about:

i) Fluid pressure and stress state at the time of vein formation (Figure 5);

ii) Dilation and slip tendency (Figures 3d and13);

iii) Failure modes for different depths in the λ_v - $\Delta\sigma$ space (Figure 14).

6.1 Mohr circle and fluid pressure

Veins in the Topinetti section formed in response to an extensional stress field (Figure 3d and Table4). Assuming an average crust density of 2700 $kgm^{-3}$and using the values obtained from $\phi=(\sigma_2-\sigma_3)/(\sigma_1-\sigma_3)$ and $R'=(P_f-\sigma_3)/(\sigma_1-\sigma_3)$listed in Table 4 (equations A3.1, A3.2a, A3.2b in Appendix 3) and equationsA3.3 (in Appendix A3), it is possible to derive the magnitude of the main stresses and of the fluid pressure at the time of vein formation (Figure 5, right panels).

In the Topinetti section, the analysis of the vein systems indicates that a very high fluid pressure ($P_f>\sigma_2$; i.e. $R'>\Phi$in Table 4) was attained at the time of sulfide, hematite and Breccia II vein formation.

6.2 Dilation and sliptendency analysis

Slip tendency and dilation tendency analysis (see Appendix A4) was performed on the faults from the Topinetti section assuming an initial friction angle of 35°, corresponding to a static coefficient of frictional sliding of 0.6 (Collettini and Sibson, 2001), and by applying the principal stress attitude and ratios derived from the analysis of vein distribution (Figure 5 and Table 4). As a first approximation, we modeled the effect of changing the friction angle for the slip and dilation tendency potential by reducing the angle of internal friction of the faulted host rock from 35° to 10° (Figure 13). The N-S, NE-SSW and NW-SE faults in Topinetti section exhibit high dilation and slip tendency values whereas the E-W faults have low probability to slip and dilate (Figure 13).

6.3 Pore fluid factor versus differential stress

Inversion of fault- and vein data (Figures 3d and 5) indicates anextensional stress field with $\sigma_v = \sigma_1$. We assume for the host rock (quartzite) of the veins filled by hematite and hematite-rich breccia (Breccia II) a density $\rho$of 2700 kgm^{-3}, a Poisson ratio ν of 0.25, a tensile strength $T$of 10-30 MPa, a cohesive strength $C$of 1-10 MPa, and a coefficient of internal friction $\mu$of 0.6-0.75 (e.g., Bieniawski, 1974;Haimson, 1980. Perras and Diederichs, 2014;Jaeger et al., 2007). Once the differential stress for depths varying between 1 and 5 km and oncethe stress ratio Φ and the stress driving ratio R' derived from the analysis of vein distribution at Topinetti are constrained(Figure 5 and Table 4),it then becomespossible to computeP_f and the λ_v for any depths.

We usedboth the empirical approach by McGarr,(1980) and the theoretical by Lisle and Sivrastava,(2004) to compute $\lambda_v$by adopting the stress ratio and the driving stress ratio derived from the analysis of vein systems (Table 4). The empirical method by McGarr,(1980) (equationA3.3 in Appendix A3)needs no a priori assumptions on rock properties,it being essentially empirical and valid for shallow crustal level (< 7 km). The resulting λ_v values vary with depth and are in the 0.74 - 0.83 range for the sulfide veins, in the 0.84 - 0.90 range for

the hematite veins and in the 0.75 – 0.84 range for the Breccia II veins (Table 5). The method by Lisle and Sivrastava,(2004) (equations A3.4a, A3.4b and A3.4c in Appendix A3) needs instead the assumption of a coefficient of friction and that the state of stress in the bedrock is at the frictional equilibrium. The obtained λ_v values do not vary with depth and are 0.80 for the sulfide veins, 0.88 for the hematite veins and 0.81 for the Breccia II veins (Table 5). Sulfide veins at the depth of 1 km (Table 5) show the lowest λ_v value according to the computation derived from both the empirical (0.74) and theoretical (0.80) method.Notably, regardless of the used method, high fluid pressure and λ_v> 0.70are common for all the three vein systems (Table 5) with the highest values computed for hematite veins (λ_v~0.9).

The possible theoretical values of failure modes for different depths are also derived by applying method of Lisle and Sivrastava, (2004; equations A3.5, A3.6 and A3.7 in Appendix A3) and then plottingthe results in λ_v - $\Delta\sigma$ space (Cox, 2010; Sibson, 2000). The λ_v for which failure can occur can bethus estimated forextensional (equation A3.5), hybrid (equation A3.6) and shear (equation A3.7) failure modes(Cox, 2010).

The λ_v values for which different modes of failure can occur at different depths are plotted(Figure 14) using the principal stress values derived by applying the theoreticalmethod(Table 4). For example, at a depth of 1 km, in order to have extensional failure (equation A35) a supra-lithostatic (λ_v> 1) fluid pressure is required (Figure 14). On the other hand, for optimally oriented faults (i.e. high angle normal faults) less than hydrostatic values (λ_v< 0.4) are required at any depths. Misoriented faults (for example, low angle normal faults) requirea fluid pressure higher than hydrostatic (λ_v> 0.4) for any depths (Figure 14). At depths of 4 and 5 km, a fluid pressure higher than hydrostatic is required only for extensional failure and misoriented faults. At depths of 2 and 3 km failure occurs for extensional and hybrid veins as well as misoriented faults for a fluid pressure higher than hydrostatic (Figure 14). The minimum values of the pore fluid factor in the Topinetti section

is observed for the sulfide veins at a depth of 1 km (λ_v = 0.74) by applying the empirical approach and (λ_v = 0.80) by applying the theoretical approach (Table 5). At depths> 1 km, for the Topinetti section the derived large fluid pressure for all the vein systems (grey stripe in Figure 14) make all failure modes possible, thus suggesting that all the faults/fractures in the rock volume at the time of vein formations were exploitable by pressurized fluids.

7. Structural and lithological control on ore deposition

In the Topinetti section fluid-rock interaction resulted in both diffuse mineralizationsandmetricmassive ore bodies. Host rock brecciation was the norm, as documented by ourmeso- and microscopic observations. Clear field relationshipsallowed usto connect brecciation to at least two distinct episodes of fluid pressureincrease, which generated Breccia I and Breccia II, respectively.

The spatial and temporal relationships between different types of hydrothermal deposits suggest that the primaryquartzite porosity mainly controlled the early sites of mineralization (i.e. at the triple junctions among quartz grains in the quartzite and quartz-breccia)during pervasive, diffuse fluid flow, leading to progressive porosity decrease due to precipitation of intergranular pyrite (Figures4a, 4b, 7a, 7b; see also Torgersen et al., 2015). On the other hand, the pattern and distribution of veins filled by pyrite, hematite and Breccia II attest to cyclic and transientepisodes of channelized fluid ingress and flow steered by the active fault systems.

In summary,sulfide, hematite and Breccia II veins associated with fault planes as well as the similarity between fracture and vein geometric attitude (Figure 3b, 3c) suggest that fluids exploited faults and associated fracture systems. Moreover, the pole to fault distribution in Figure 13 suggests that N-S and NE-SW faults were the main sites exploited by fluids during extension. Based on the evidence presented above, the observed relative timing of faulting

(with the E-W faults being the youngest) is in agreement with the results of dilation and slip tendency analysis.

The association between faults, fractures and mineralized fluids can be alternatively explained by: i) initial fault nucleation and propagation, which triggered the ingress of a first batch of fluid during dilatant, pressure-sensitive deformation followed by more fluid batches entering the actively deforming faults and interacting repeatedly with the host rock causing renewed hydrofracturing, veining and brecciation (Figure 4g), orii) an initial overpressured batch of fluid infiltrating the entire rock volume by generating a diffuse fracture network by hydrofracturing and by possibly reactivating suitably oriented pre-existing faults and fractures. The fact that Breccia II veinletsare alongslikensided fault planesand that hematite veins cut across fault planes at high angle suggests multiple episodes of fluid circulation. Moreover, faulting affected the large body of Breccia II and the massive ore bodies, with a maximum displacement of up to 20 m, suggesting that deformation continued after the mineralizing event had ceased.

The pore fluid factor derived from the analysis of vein distribution suggests that all fractures and faults were prone to easy reactivationbecause of the high fluid pressure of the system (Figure 14),as also confirmed bythe slip tendency analysis on the collected fault data (Figure 13).

Clark et al. (1995) proposed a power-law distribution of vein thickness if a constant vein nucleation rate occurrs with a time-averaged growth rate proportional to thickness. A negative exponential distribution for the vein thickness is expected for a constant vein growth rate. Hooker et al. (2014) suggested that the power-law size distribution for fractures derives from the interaction among growing fractures with large fractures inhibiting the growth of smaller ones.

Foxford et al., (2000) observed non-power law vein thickness distribution in the W±Sn-

bearing quartz veins hydrothermal system in Minas da Panasqueira (Portugal). Deviations from a power-law behavior were ascribed to competitive vein growth that would provide mechanisms for inhibiting vein nucleation and for localizingdeformation onto a few evenly spaced veins. These mechanisms account for vein opening histories whereby initial crack–seal growth is superseded by rapid vein opening (Foxford et al., 2000). Moreover, veins confined in mechanical/stratigraphic layers (i.e. stratabound veins) have generally negative exponential or log-normal thickness distributions, while a power-law distribution of thickness is generally observed for non-stratabound veins (Gillespie et al., 1999).

Our analysis of the vein thickness size distribution (Table 2) suggests that:

i) the high (> 1) fractal exponent for the thickness distribution of sulfideveins is consistent with a hydrothermal origin of the veins, with fluids derived from sources external from the host rock;

ii) the negative exponential distributionof the thickness of the hematite-veins andofBreccia II-veins suggests that these vein systems were confined within the quartzite (i.e. strabound) with fluid source external to the host rock.

The particle size analysis of Breccia II documents its possible genesis as due to corrosive wear and volume expansion (Figure 12) according to the model by Jébrak (1997). The occurrence of a trade-off length (higher than the grinding limit) at the micro and meso scale for Breccia II (Table 3 and Figure 11) may suggest that the change in slope in the fractal dimension reflects a change in the dominant mechanism of brecciation. According to this interpretation, we suggest that shear deformation dominatedduring the initial stage of vein formation asdocumented by the low D_s values (< 1.5- 2) and high D_r values (> 1.2). This was followed by a phase of deformation caused byhigh fluid pressure leading to hydrofracturing and volume expansion, causing high D_s values (> 2—2.5; Table 3 andFigure 11).

In summary, geological, structural, mineralogical and textural constraints argue for the followingconceptual evolutionary model for the genesis of the Topinettimineralized system:

1) During the initial stages of mineralization, brittle extensional faulting created efficient paths for fluid ingress, migration and accumulation within the host porous quartzite. Pervasive fluid flow caused the growth of intergranular pyrite within the quartzite and micro conglomerate of theAnageniti minute Member of the Verruca Formation, leading to a decrease of the host rock bulk primary permeability (Figure 15a).

2) Theprogressive decrease of permeability accompanied by continuous fluid ingress along dilatant fault planes led to a strong increase of fluid pressure favoring the overall embrittlement of the rock and its eventual mechanical failure with the formation of a first generation of breccia (Breccia I), withclastsof pyrite-bearingquartzite embedded within a massive sulfide matrix (Figure 15b).

3) Ingress of a distinct Fe-bearing ore fluid still associated with continued faulting would have further evolved the mineralization process. This new fluid causedthe formation of Breccia II, circulation of iron and sulfide rich fluidsand the deposition of thestrataboundlarge hematite ore bodies (> 5 m in size) in the VerrucaFormation quartzite (Figure 15c).

In this conceptual model, continuous and probably cyclic feedback between faulting and fluid pressure variations is recorded by the relationships between Breccia II veins and faults (i.e. pore fluid-time cartoons in Figure 15). Cyclic episodes of pore pressure build up and faultingare testified to by the genetic relationships documented between faults and hematite veins and Breccia II. Indeed, different generations of hematite veins arecommonly observed on- or in the proximity of the same fault plane to form slikensides but also to cut at high angle the fault. As pointed out by our dilation and slip tendency analysis (Figure 13), N-S to NE-SW faults where optimally oriented during fluid venting and most hematite veins and Breccia II are along these faults and the associated fractures.

8. Conclusion

The studied hydrothermal system represents a clear case of macro- to mesoscale fluid circulation in a homogeneous lithological system characterized by both pervasive and channelized circulation. The former is controlled by the primary lithological characteristics of the sedimentary host rock, the latter by deformation (faulting)-induced dilation and transient overpressure conditions.

The feedback between fluid and deformation during ore body formation is well recorded along the Topinetti section and geological and structural observationsdocument that:

1)Initial pervasive ingress of sulfide rich fluids with growth of intergranular pyrite caused significant permeability reduction of the host rock (massive to coarsely parallel-stratified white-grey quartzite and quartzitic breccia with growth of intergranular pyrite) and steers the sites where veining, brecciation and mineralization developed;

2) Coeval faulting favouring the influx of large amounts of mineralizing fluids led to further veining and brecciation that controlled the transition from pervasive to channellized circulation.

3) Faulting favoured the influx of large amounts of mineralizing fluids that led to veining and brecciation.

4) At least two cyclic episodes of pore pressure build up, faulting, fluid venting and fast pressure release (i.e. veining and brecciation) account well for all the observed structural and mineralogical features of the area.

The reported structural and geologic data allow us to propose an evolutionary conceptual schemefor the mineralizationsof the mining district of the eastern Island of Elba. That scheme might be regarded as reliable also forother, upper crustal Late Miocene-Pliocene ore mineralizations of the northern Apennines.

Appendix A. Methods used for defining stress state and breccia genesis

A.1 Vein thickness size distribution

Power law or negative exponential distributions well describe the distribution of vein thickness (e.g., Mazzarini et al., 2014 and references therein). Power-law distribution is defined as $N(>w)=cw^{-a}$ where c is a normalization constant, w is the vein thickness (or aperture or width) and a is the power law exponent. A negative exponential distribution is defined by $N(>w)=ce^{-aw}$ where c and a are the distribution parameters.

The following points should be considered when determining the distribution parameters: (1) the error associated with the resolution limit of the measurements (truncation), and (2) the error resulting from values of the measured features extending beyond the sampling window (censoring). The effect of truncation is the underestimation of thecontributions of measurements (e.g., thickness) below the resolution of the acquisition method (for example, veins with a thickness lower than 0.5 mm). The effect of censoring is the underestimation of measurements extending beyond the sampling window (e.g., a thickness greater than the area of the thin section used to perform the measurement). Comparison of the theoretical maximum values of the distribution (wmax) with the maximum sampled value can thus give an indication of the influence of censoring and truncation; the higher the difference between these values, the higher is the influence of under-sampling. The theoretical maximum thickness could be derived by imposing N(wmax)=1 and solving for w (e.g., Mazzarini et al., 2011).

A.2 Particle Size Distribution (PSD)

A power law (fractal) distribution has been show to characterize the fragment size distribution of brittle fault rocks including hydrothermal breccias with variable values of the fractal exponents (e.g. Jébrak, 1997; Clark and James, 2003, Keulen et al., 2007).

Two geometric parameters appear to be particularly suitable to the purpose of discriminating

the mechanisms responsible for brecciation (Jébrak, 1997; Clark and James, 2003), 1) the fragment geometry exponent (D_r) and 2) the fragment size distribution exponent (D_s). D_r describes how regular the shape of a fragment is, whereas D_s describes the probability that a certain size is represented in the analyzed population of fragments.

The easiest method to compute the fragment geometry dimension (D_r) is by applying the "box-counting" method (Mandelbrot, 1982), which is run by placing a grid of finite box sizes on the outline of the fragment and by counting the intersections between the boundaries of the fragment and the grid. Varying the box sizes in the grid generates a different number of intersections. We used the tools in FracLab of ImageJ (https://imagej.nih.gov/ij/) to apply the counting box method. The more irregular the boundary, the higher the resulting D_r; for example, a well-rounded fragment will yield a low D_r for the simplicity of its shape, whereas a fragment that has undergone chemical or corrosive wear causing an irregular and less spherical shape will yield an higher D_r value.

The fragment size distribution D_s is computed by analyzing the cumulative distribution of measured fragment sizes by applying the equation $N(>r) = cr^{-D}$, where r is the size of the fragment, c is a normalization constant, $N(>r)$ is the number of fragments of radius greater than r, and D is the fractal dimension (D_s).

As a power-law distribution, on a log–log plot of cumulative fragment frequency vs. fragment radius, a fractal distribution appears as a straight line with a slope of D_s; the higher the D_s value, the higher the amount of small fragments.

The fragment size distribution curve of breccias is often characterized by a change in slope defined by a trade-off length (r_k), which is generally attributed to a change in the dominant comminuting mechanism (e.g., Keulen et al., 2007).

A.3. *Mohr circle and fluid pressure*

Three angles are used to describe the distribution of the poles to the veins in the analysis by

Jolly and Sanderson (1997): θ_1 is the angle between the σ_2 stress axis and the border of the vein pole distribution in the σ_2 - σ_3 plane; θ_2 is the angle between the σ_1 stress axis and the border of the vein pole distribution in the σ_1- σ_3 plane, and θ_3 is the angle between the σ_1 stress axis and the border of the vein pole distribution in the σ_1- σ_2 plane.

According to Jolly and Sanderson, (1997) the driving stress ratio R' is a function of the θ_2 angle:

$$R'=(1+\cos 2\theta_2)/2 \qquad \text{(A3.1)}$$

And the stress ratio Φ is a function of the θ_2 and $\theta_1$angles for $P_f<\sigma_2$ and of the θ_2 and $\theta_3$angles for $P_f>\sigma_2$:

$$\Phi = (1+\cos 2\theta_2)/(1+\cos 2\theta_1) \qquad \text{A3.2a}$$

$$\Phi = [1-(1-\cos 2\theta_2)/(1-\cos 2\theta_3)] \qquad \text{A3.2b}$$

In case of an extensional stress field, $\sigma_v = \sigma_1 = \rho g z$ where ρ is the rock density (kgm^{-3}), g the gravity (ms^{-2}) and z the depth in meters. The ratio of fluid pressure to the vertical stress (lithostatic load for an extensional stress field) is the pore fluid factor $\lambda_v = P_f/\sigma_v$ (e.g. Sibson 2000) where P_f is the fluid pressure and σ_v is the vertical lithostatic stress.

If the differential stress is constrained it is then possible to infer the values of the principal stresses by two possible approaches:

1) At crustal depths < 7 km, by using the relation $2\tau_m = \Delta\sigma$, McGarr (1980) provided the following empirical relationship correlating differential stress $\Delta\sigma$ and shear stress τ_m to depth z (in kilometers):

$$\tau_m = 5.0 + 6.6z \qquad \text{(A3.3)}$$

2) Lisle and Srivastava (2004), proposed the following theoretical relationships for computing the principal stress values, assuming that *i)* the Mohr circle is tangential to the Mohr-Coulomb failure curve, and *ii)* the state of stress is at frictional equilibrium:

$$\sigma_1 = 0.5k(1+1/\sin\alpha) \quad \text{(A3.4a)}$$

$$\sigma_2 = \sigma_1 - k(1-\phi) \quad \text{(A3.4b)}$$

$$\sigma_3 = \sigma_1 - k \quad \text{(A3.4c)}$$

where α is the angle of internal friction, ϕ the stress ratio and k is a parameter describing the Mohr circle geometry.

The theoretical values of failure modes for different depths can be plotted in the λ_v - $(\sigma_1 - \sigma_3)$ space (Cox, 2010; Sibson, 2000) where the following cases are considered:

i) Extensional failure:

$\sigma_1-\sigma_3 < 4T$ and $\lambda_v = (\sigma_3 + T)/\sigma_v$; (A3.5)

ii) Hybrid failure:

$4T < \sigma_1-\sigma_3 < 5.66T$ and $\lambda_v = \sigma_3/\sigma_v + [8T(\sigma_1-\sigma_3) - (\sigma_1-\sigma_3)^2]/16T\sigma_v$; (A3.6)

iii) Shear failure:

$\sigma_1-\sigma_3 > 5.66T$ and $\lambda_v = 1/2\mu\sigma_v[2C+\mu(\sigma_1+\sigma_3) - \mu(\sigma_1-\sigma_3)\cos 2\theta_r - (\sigma_1-\sigma_3)\sin 2\theta_r]$; (A3.7)

θ_r is the angle between the fault plane and σ_1, which in an extensional regime is 30° for favorably oriented (steep) faults and 60° for misoriented (low angle) faults.

A.4. *Dilation and slip tendency analysis*

Slip tendency (T_s) is the dimensionless ratio of maximum resolved shear stress to normal stress (τ/σ) acting on a surface and is therefore a function of the orientation of the surface of interest and the form of the stress tensor (Morris et al., 1996). Slip tendency analysis provides insights into the distribution of past slip on faults and fractures (Collettini and Trippetta, 2007; Morris et al., 2016). The dilation of faults and fractures is controlled by the resolved normal stress, which is a function of the lithostatic and tectonic stresses and fluid pressure. The normal stress can be normalized by comparison with the differential stress to give the dilation tendency (T_d) for a surface of given orientation defined as $T_d = (\sigma_1-\sigma_n)/(\sigma_1-\sigma_3)$ where σ_n is the stress normal to the surface (Ferrill et al., 1999; Ferrill et al., 2017).

References

Aldinucci,M., Gandin,A., Sandrelli,F., 2008. The Mesozoic continental rifting in the Mediterranean area: insights from the Verrucanotectofacies of southern Tuscany (Northern Apennines, Italy). Int. J. Earth Sci., 97, 1247–1269.

Andre´-Mayer, A-S., Sausse, J., 2007. Thickness and spatial distribution of veins in a porphyry copper deposit, Rosia Poieni, Romania. Journal of Structural Geology, 29, 1695-1708.

Anonymous, 1943. Miniera di Rio Albano dal 1894 al 1943. Volume 31: Firenze, Corpo Reale delle Miniere, p. 1-65.

Bieniawski, Z.T., 1974. Estimating the strength of rock materials. Journal of the South African Institute of Mining and Metallurgy, 3, 312-320.

Becker, S.P., Eichhubl, P., Laubach, S.E., Reed, R.M., Lander, R.H., Bodnar, R.J., 2010. A 48 m.y. history of fracture opening, temperature, and fl uid pressure: Cretaceous Travis Peak Formation, East Texas basin. GSA Bulletin; 122, 7/8, 1081–1093, doi: 10.1130/B30067.1.

Bertini, G., Casini, M., Gianelli, G., Pandeli, E., 2006.Geological structures of a long-living geothermal system, Larderello, Italy. Terra Nova, 18, 163–169.

Blenkinsop, T.G., 1991. Cataclasis and processes of particle size reduction. Pure and Applid Geophysics, 136, 59-86.

Bodechtel, J., 1965. ZurGenese der Eisenerze der Toskana und der Insel Elba: NeuesJahrbuchfürMineralogie - Abhandlungen, 103, 2, 147–162.

Bonnet, E., Bour, O., Odling, N.E., Davy, P., Main, I.,Cowie, P., Berkowitz, B., 2001. Scaling of fracture systems in geological media: Reviews of Geophysics, 39, 347–383, doi: 10.1029/1999RG000074.

Bons, P.D., 2001. The formation of large quartz veins by rapid ascent of fluids inmobile hydrofractures.Tectonophysics, 336, 1-17.

Bortolotti, V., Fazzuoli, M., Pandeli, E., Principi, G., Babbini, A., Corti, S., 2001. Geologyof central and eastern Elba Island, Italy.Ofioliti, 26, (2a), 97–150.

Calanchi, N., Dal Rio, G., Prati, A., 1976. Miniere e minerali dell'Elba orientale.

Cataldi, R., Lazzarotto, A., Muffler, P., Squarci, P., Stefani, G., 1978. Assessment of geothermal potential of central and southern Tuscany.Geothermics, 7, 91-131.

Clark, C., James, P., 2003. Hydrothermal brecciation due to fluid pressure fluctuations: examples from the Olary Domain, South Australia. Tectonophysics, 366, 187– 206.

Clark, M.B., Brantley, S.L., Fisher, D.M., 1995. Power-law vein-thickness distribution and positive feedback in vein growth. Geology 23, 975–978.

Collettini, C., Sibson,R.H., 2001. Normal faults, normal friction? Geology, 29 (10), 972-930.

Collettini, C., Trippetta, F., 2007. A slip tendency analysis to test mechanical and structural control on aftershock rupture planes. Earth and Planetary Science Letters, 255, 402–413.

Cox, S.F., 1995. Faulting processes at high fluid pressures: An example of fault valve behaviour from the Wattle-Gully Fault, Victoria, Australia. Journal of Geophysical Research, 100, 841-859.

Cox, S.F., Knackstedt, M.A., Braun, J., 2001. Priciples of structural control on permeability and fluid flow in hydrothermal systems. Reviews in Economic Geology, 14, 1-24.

Cox, S.F., 2010. The application of failure mode diagrams for exploring the roles of fluid pressure and stress states in controlling styles of fracture-controlled permeability enhancement in faults and shear zones. Geofluids, 10, 217-233.

Cox, S.F., Munroe, S.M., 2016. Breccia formation by particle fluidization in fault zones:

implications for transitory, rupture controlled fluid flow regimes in hydrothermal systems. American Journal of Science, 316, 241–278, DOI 10.2475/03.2016.02.
Della Vedova, B., Vecellio, C., Bellani, S., Tinivella, U., 2008. Thermal modelling of the Larderellogeothermalfield (Tuscany, Italy). Int. J. Earth.Sci. (GeolRundsch), 97, 317–332.
Deschamps, Y., Dagallier, G., Macaudiere, J., Marignac, C., Saupe, F., 1983a. Le gisement de pyrite-hématite de Valle Giove (Rio Marina, Ile d'Elbe, Italie): (Contribution à la connaissancedesgisements de Toscane - I), Partie 1: SchweizerischeMineralogische und PetrographischeMitteilungen, 63, 149-165.
Deschamps, Y., Mecaudiere, J., Marignac, C., Moine, B., Saupe, F., 1983b. Le gisement de pyrite-hématite de Valle Giove (Rio Marina, Ile d'Elbe, Italie) : (Contribution à la connaissancedesgisements de Toscane -I), Partie 2: SchweizerischeMineralogische und PetrographischeMitteilungen, 63, 301-327.
Dini, A., Innocenti, F:, Rocchi, S., Tonarini, S., Westerman, D.S., 2002.The magmatic evolution of the late Miocene laccolith–pluton–dyke granitic complex of Elba Island, Italy. Geol. Mag., 139, 257–279.
Dini, A., Mazzarini, F., Musumeci, G., Rocchi, S., 2008. Multiple hydro-fracturing by boron-rich fluidsin the late Miocene contact aureole of easternElba Island (Tuscany, Italy). Terra Nova, 20, 318-326.
Dünkel, I., 2002. The genesis of East Elba iron ore deposits and their interrelation with Messinian tectonics". PhD. Thesis, TübingerGeowissenschaftlicheArbeiten, A, 65, 282 pp.
Durr, N., Sauer, M., 2015. Mesoscale modeling of quartzite and sandstone under shock loading: Influence of porosity and pressure-dependent quartz stiffness on macroscopic behavior. Procedia Engineering, 103, 105 – 112.
Ferrill, D.A., Winterle, J., Wittmeyer, G., Sims, D., Colton, S., Armstrong, A., Morris, A.P., 1999. Stressed rock strains groundwater at Yucca Mountain, Nevada. GSA Today, 9 (5), 1-8.
Ferrill, D.A., Evans, M.A., McGinnis, R.N., Morris, A.P., Smart, K.J., Wigginton, S.S., Gulliver, K.D.H., Lehrmann, D., de Zoeten, E., Sickmann, Z., 2017. Fault zone processes in mechanically layered mudrock and chalk. Journal of Structural Geology, 97, 118-143.
Foxford, K.A., Nicholson, R., Polya, D.A., Hebblethwaite, R.P.B., 2000. Extensional failure and hydraulic valving at Minas da Panasqueira, Portugal: evidence from vein spatial distributions, displacements and geometries. Journal of Structural Geology, 22, 1065-1086.
Gillespie, P.A., Johnston, J.D., Loriga, M.A., McCaffrey, K.J.W., Walsh, J.J., Watterson, J., 1999. Influence of layering on vein systematics in line samples. In: McCaffrey, K.J.W., Lonergan, L., Wilkinson, J.J. (Eds.), Fractures, Fluid Flow and Mineralization, 155. Geological Society Special Publication, London, 35–56.
Gilliéron, F., 1959. Osservazioni sulla geologia dei giacimenti di ferro dell'Elba orientale. Industria Mineraria, v. X, no. 1, 1-10.
Gudmundsson, A., 2011. Rock Fractures in Geological Processes. Cambridge University Press, UK, pp. 578.
Haimson, B.C., 1980. Near-surface and deep hydrofracturing stress measurements in the Waterloo Quartzite. Int. J. Rock Mech. Min. Sci. & Geomech. Abstr., 17, 81-88.
Hooker, J.N., Laubach, S.E., Marrett, R., 2014. A universal power-law scaling exponent for fracture apertures in sandstones. GSA Bulletin, 126, 9/10, 1340–1362, doi: 10.1130/B30945.1.
Hooker, J.H., Larson, T.E., Eakin, A., Laubach, S.E., Eichhubl, P., Fall, A., Marrett, R., 2015.

Fracturing and fluid flow in a sub-décollement sandstone; or, a leak in the basement. Journal of the Geological Society, 172, 428-442, doi:10.1144/jgs2014-128.
Hubbert, M.K., Willis, D.G., 1957.Mechanics of hydraulic fracturing.Trans. Am. Inst. Mech. Eng., 210,153–168.
Keller, J.V.A., Coward, M.P., 1996. The structure and evolution of the northernTyrrhenian Sea. Geol. Mag., 103, 1–16.
Kendall, K., 1978. The impossibility of comminuting small particles by compression. Nature, 272, 710-711.
Keulen, N., Heilbronner, R., Stünitz, H., Boullier, A-M., Ito, H., 2007.Grain size distributions of fault rocks: A comparison between experimentally and naturally deformed granitoids. Journal of Structural Geology, 29, 1282-1300.
Kim, K, Kemeny, J., Nickerson, M., 2014. Effect of rapid thermal cooling on mechanical rock properties. Rock Mech. Rock Eng., 47, 2005–2019.
Jaeger, J.C., Cook, N.G.W., Zimmerman, R., 2007. Fundamentals of Rock Mechanics, 4th Edition. Wiley-Blackwell, pp. 488.
Jébrak, M., 1997. Hydrothermal breccias in vein-type ore deposits: A review of mechanism, morphology and size distribution. Ore Geology Reviews, 111-134.
Johnston, J.D., McCaffrey, K.J.W., 1996. Fractal geometries of vein systems and the variation of scaling relationships with mechanism. J. Struct. Geol. 18, 349–358.
Jolly, R.J.H., Sanderson, D.J., 1997.A Mohr circle construction for theopening of a pre-existing fracture. Journal of Structural Geology, 19, 887-892.
Lander, R.H., Laubach, S.E:, 2015. Insights into rates of fracture growth and sealing from amodel for quartz cementation in fractured sandstones.GSA Bulletin, 127, 3/4, 516–538, doi:10.1130/B31092.1.
Lippolt, H.J., Wernicke, R.S., Bahr, R., 1995. Parageneticspecularite and adularia (Elba, Italy): Concordant (U+Th)-He and K-Ar ages. Earth Planetary Science Letters, 132, 43-51.
Lisle R.J., Srivastava, D.C., 2004. Test of the frictional reactivation theory for faults and validity of fault-slip analysis. Geology, 32(7); 569–572; doi: 10.1130/G20408.1.
Loriga, M.A., 1999. Scaling systematics of vein size: an example from the Guanajuato mining district (Central Mexico). In: Mc Caffrey, K.J.W., Lonergan, L., Wilkinson, J.J. (Eds.), Fractures, Fluid Flow and Mineralization, 155. Geological Society Special Publications, London, pp. 57–67.
Lotti, B., 1886. Descrizione geologica dell'isola d'Elba. Roma, Tipografia nazionale, Memorie Descrittive della Carta Geologica d'Italia, v. 2-4.
Lotti, B., 1910, Geologia della Toscana. Roma, Tipografia Nazionale, Memorie Descrittive della Carta Geologica d'Italia, p. 1-484.
Mandelbrot, B.B.,1982. The Fractal Geometry of Nature. W. H. Freeman, New York.
Manger, G.E., 1963. Porosity and bulk density of sedimentary rocks. Geological Survey Bulletin, 1144-E, 1-60.
Marrett, R.A., Allmendinger, R.W., 1990. Kinematic analysis of fault-slip data. Journal of Structural Geology, 12, 973-986.
Massa, G., Musumeci, G., Mazzarini, F., Pieruccioni, D., 2017. Coexistence of contractional and extensional tectonics during the northern Apennines orogeny: the late Miocene out-of-sequence thrust in the Elba Island nappe stack. Geological Journal, 52, 353–368.
Mazzarini, F., Isola, I., Ruggieri, G., Boschi, C., 2010. Fluid circulation in the upper brittle crust: thickness distribution, hydraulic transmissivity fluid inclusion and isotopic data of veins hosted in the Oligocene sandstones of the Macigno Formation in southern Tuscany, Italy. Tectonophysics, 493, 118-138.
Mazzarini, F., Musumeci, G., Cruden, A.R., 2011. Vein development during folding in the

upper brittle crust: The case oftourmaline-rich veins of eastern Elba Island, northern Tyrrhenian Sea, Italy. Journal of Structural Geology, 33, 1509-1522.
Mazzarini, F., Ruggieri, G., Isola, I., Boschi, C., Dini, A., Musumeci, G., Rocchi, S., 2014. Fluid transfer and vein thickness distribution in high and low temperature hydrothermal systems at shallow crustal level in southern Tuscany (Italy). Annals of Geophysics, 57, 3, 2014, S0326, doi:10.4401/ag-6263.
McGarr, A., 1980. Some constraints on levels of shear stress in the crust from observations and theory. Journal of Geophysical Research, 85, B1, 6231-6238.
Morris, A., Ferrill, D.A., Henderson, D.B., 1996. Slip-tendency analysis and fault reactivation.Geology, 24 (3), 275–278.
Morris, A.P., Ferrill, D.A., McGinnis, R.N., 2017. Using fault displacement and slip tendency to estimate stress states . Journal of Structural Geology, 83, 60-72.
Musumeci, G., Vaselli, L., 2012. Neogene deformation and granite emplacement in the metamorphic units of northern Apennines (Italy): insights from mylonitic marbles in the Porto Azzurro pluton contact aureole (Elba Island). Geosphere, 8 (2), 470–490.
Musumeci, G., Mazzarini, F., Cruden, A.R., 2015. The Zuccale Fault, Elba Island, Italy: A new perspective from fault architecture. Tectonics, 34, 1195–1218.
National Research Council, 1996. Rock Fractures and Fluid Flow: Contemporary Understanding and Applications. Washington, DC: The National Academies Press. https://doi.org/10.17226/2309.
Nishiyama, T., 1989. Kinetics of hydrofracturing and metamorphic veining. Geology, 17, 1068-1071.
Oliver, N.H.S., 1996. Review and classification of structural controls on fluid flow during regional metamorphism. J. Metamorphic Geol., 14, 477–492.
Papeschi, S., Musumeci, G., Mazzarini, F., 2017. Heterogeneous brittle-ductile deformation at shallow crustal levels underhigh thermal conditions: The case ofa synkinematic contact aureole in theinner northern Apennines, southeastern Elba Island, Italy.Tectonophysics, 717, 547–564.
Perras, M.A., Diederichs, M.S., 2014. A Review of the Tensile Strength of Rock: Concepts and Testing. Geotech. Geol. Eng., 32, 525–546.
Pertusati, P.C., Raggi, G., Ricci, C.A., Duranti, S., Palmeri, R., 1993. Evoluzione postcollisionale dell'Elba centro-orientale. Mem. Soc. Geol. Ital. 49, 297–312.
Philipp, S.L., Afsar, F., Gudmundsson, A., 2013. Effects of mechanical layering on hydrofracture emplacement and fluid transport in reservoirs. Front. EarthSci. 1, 4, doi:10.3389/feart.2013.00004.
Poelchau, M.H., Kenkmann, T., Hoerth, T., Schäfer, S., Rudolf, M., Thoma, K., 2014. Impact cratering experiments into quartzite, sandstone and tuff: The effects of projectile size and target properties on spallation. Icarus, 242, 211-224.
Ramsay, J.G., 1980. The crack-seal mechanism of rock deformation.Nature, 284, 135-139.
Rau, A., Tongiorgi, M., 1974. Geologia dei Monti Pisani a Sud-Est della Valle del Guappero. Mem. Soc. Geol. It., 13, 227–408.
Roberts, S., Sanderson, D.J., Gumiel, P., 1999. Fractal analysis and percolation properties of veins. In: McCaffrey, K.J.W., Lonergan, L., Wilkinson, J.J. (Eds.), Fractures, Fluid Flow and Mineralization, 155. Geological Society Special Publication, London. 71-16.
Sammis, C., King, G., Biegel, R., 1987.The kinematics of gouge deformation. Pure and Applied Geophysics, 125, 777-812.
Sammis, C.G., Biegel, R.L., 1989. Fractals, fault-gouge, and friction. Pure and Applied Geophysics, 131, 255-271.
Scholz, C.H., 1987. Wear and gouge formation in brittle faulting. Geology, 15, 493-495.
Sibson, R.H., 1986. Earthquakes and rock deformation in crustal fault zones.Ann. Rev. Earth

Planet. Sci., 14, 149-75.
Sibson, R.H., 2000. Fluid involvement in normal faulting.Journal of Geodynamics, 29, 469-499.
Sillitoe, R.H., 1985. Ore-RelatedBreccias in volcanoplutonicarcs.EconomicGeology, 80, 1467-1514.
Tanelli, G., Benvenuti, M., Costagliola, P., Dini, A., Lattanzi, P., Maineri, C., Mascaro, I., Ruggieri, G., 2001. The ironmineraldeposits of Elba island: state of the art. Ofioliti, 26, 239-248.
Torgersen, E., Viola, G., Sandstad, J.S., Stein, H., Zwingmann, H., Hannah, J., 2015. Effects of frictional–viscous oscillations and fluid flow events on the structural evolution and Re–Os pyrite–chalcopyrite systematics of Cu-rich carbonate veins in northern Norway. Tectonophysics, 659, 70-90.
Viola, G., Kounov, A., Andreoli, M.A.G., Mattila, J., 2012. Brittle tectonic evolution along the western margin of South Africa: More than 500 Myr of continued reactivation. Tectonophysics, 514, 93-114.
Viola, G., Torgersen, E., Mazzarini, F., Musumeci, G., van der Lelij, R., Schönenberger, J., Garofalo, P.S., 2018. New Constraints on the Evolution of the Inner Northern Apennines by K-Ar Dating of Late Miocene-Early Pliocene Compression on the Island of Elba, Italy. Tectonics, 37, 3229–3243, https://doi.org/10.1029/2018TC005182.
Walton, W.H., 1948. Feret's statistical diameter as a measure of particle size.Nature, 162, 329-330.
Zitzmann, A., 1977, The iron ore deposits of Italy, in Walther, H. W., and Zitzmann, A., eds., The Iron ore deposits of Europe and adjacent areas, Volume 1: Hannover, BundesanstaltfuerGeowissenschften und Rohstoffe, p. 209-218.

FIGURE CAPTIONS

Figure 1. **a)** Geological map of the Island of Elba (modified from Papeschi et al., 2017); red box: location of Figure 1b; the inset shows the location of the island. **b)** Geologic sketch map of the Rio Albano area in the eastern Isand of Elba (modified form Massa et al., 2017); red ellipse: location of Figure 2. **c)** WNW-ESE geologic section across the eastern Island of Elba (modified after Massa et al. 2017; A-B trace and color code as in Figure 1b).

Figure 2.a) Google Earth© image of the Topinetti coastal section; digits 1, 2 and 3 refer to the southern, central and northern sectors discussed in the main text. **b)** Geological sketch map of the Topinetti section.

Figure 3. Stereographic projection (lower hemisphere) of structural data from the Topinetti coastal section. **a)** Poles to bedding planes and fold axis; **b)**Poles to extensional fractures; **c)**Poles to veins (grey squares: sulfide veins; open triangles: hematite veins; black dots: Breccia II veins). **d)**Faults with hanging wall slip direction (arrows) and the overall plane solution derived from the fault kinematic analysis; red squares are principal stresses (trend/plunge) derived from fault inversion (**1:**σ_1: N151°E 87°SE; **2:**σ_2: N0°E 3°N; **3:** σ_3: N90°E 1°W). Underlying grey beach ball are from the right-dihedral analysis of faults; all inversion analysis have been made by using using FaultKin by R.W. Allmendinger (Marret and Allmendinger, 1990)

Figure 4. a) Quartzite hosting mineralizations with pyrite (white shiny dots), coin diameter is 19 mm. **b)** Thin section of quartzite (white scale is 2 mm long). Note the occurrence of inter-granular pyrite. **c)** Sulfide veins in quartzite, coin diameter is 26 mm. **d)** Thin section of sulfide vein in fine-grained quartzite (white scale is 0.5 mm long). **e)** Hematite veins in stratified quartzite and quartz breccia, white scale is 45 cm long. **f)** Thin section of hematite veins (white scale is 2 mm long); note the localized brittle deformation of the host rock with clasts embedded in a very fine dark hematite-rich matrix. **g)** Breccia with hematite (Breccia II) injected within the quartzite and quartz breccia forming veins with evident hydrofracturing; compass for scale (6.5 cm in size). **h)** Thin section of Breccia II with clasts of quartz within a very fine dark hematite-rich matrix (white scale is 0.5 mm long).

Figure 5. *Left panels*:Poles to vein distribution (lower hemisphere stereonet) contoured by using the Kamb exponential method (maximum class >21 data). Red diamond: σ_3; green circle: σ_2; blue circle: σ_1. *Right panels*: Mohr plot (derived following Jolly and Sanderson, (1997) from ϕ and R' as per Table1 (see Appendix A3); light grey shaded areas represent

fluid pressure P_f relationships with principal stresses. **a)** Sulfide veins, **b)** hematite veins and **c)** Breccia II veins.

Figure 6. **a)** Breccia I consists of quartzite clasts embedded in a matrix consisting of quartz, chlorite, pyrite and minor hematite, white bar is 22 cm long. **b)** Breccia II ismade up of clasts of quartzite and Breccia I within a matrix consisting of quartz and hematite, white bar is 30 cm long. **c)** Massive 2 m thick hematite ore body resting on Breccia II. **d)** East-dipping low angle normal fault cutting across Breccia II with slikenline; backpack for scale. **e)** Panorama looking north, with ore bodies (yellow arrow) cut by a low angle fault (white arrow). **f)** East-dipping high angle fault with hematite along the fault plane, compass for scale (6.5 cm in size).

Figure 7. Photomicrographs showing the microtextural characteristics of the pyrite-bearing Breccia I and hematite Breccia II. **a)** Transmitted light photomicrographs showing the contrast between a newly formed euhedral quartz crystal (Qtz1), which is texturally associated with pyrite, and deformed anhedral quartz from the host rock (Qtz); white bar is 1000 μm long. **b)** Reflected light photomicrograph documenting two generations of pyrite, one coarse grained and euhedral (Py1) and a second fine grained and subhedral/anhedral (Py2). The second generation overgrows and fills late crosscutting veins thus postdating the first one. **c)** Transmitted light photomicrographs showing the newly formed euhedral quartz (Qtz1) juxtaposed against the anhedral quartz from the host rock (Qtz); white bar is 200 μm long. **d)** Reflected light photomicrograph showing that this breccia is made of an aggregate of elongated euhedral hematite (Hem) platelets forming a boxwork texture.

Figure 8. a) Stereonet, lower hemisphere, of poles to extensional fractures (black dots) vs. pole to faults (open circles). **b)** Stereonet, lower hemisphere, of poles to sulfide veins (black diamonds) vs. poles to fault (open circles). **c)** Stereonet, lower hemisphere, of poles to hematite veins (black diamonds) vs. poles to fault (open circles). **d)** Stereonet, lower hemisphere, of poles to Breccia II veins (black diamonds) vs. poles to fault (open circles). **e)** High angle, east-dipping normal fault cutting across the Breccia II with growth of hematite fibres. **f)** Photomosaic of east-dipping low angle normal fault (black arrow) and associated high angle extensional fractures and faults (white arrow) decorated with Breccia II. White box is Figure 8g. **g)** Zone of junction between a low angle fault and an associated high angle fault (arrows indicate the sense of slip). In the jog between the faults there occurs a large amount of Breccia II. **h)** High angle, east-dipping normal fault with slikenlines on the fault plane in quartzite and quartz breccia with 4 cm thick Breccia vein along the fault plane. Coin diameter is 22.3 mm.

Figure 9. Results of the vein thickness size distribution analysis (see Appendix A1). Grey areas represent the range of thickness (i.e. size range) for which the fit is computed. *Left panels:* histograms of the thickness distribution with bin size of 5 mm. *Right panels:* log-log plot of N(w) v.s. w (mm) where N(w) is the number of veins with thickness greater than w. **a)** Sulfide veins; **b)** Hematite veins; **c)** Breccia II veins.

Figure 10. Photographs used for the PSD (Particle Size Distribution) analysisof Breccia II at the meso- and micro-scale. **a)**Photographs of the outcrop (sample 407), horizontal dimension is 32 cm; **b)**Photographs of the outcrop (sample 398), horizontal dimension is 20 cm; **c)**Photographs of the thin section (sample 39), photo horizontal dimension is

11 mm. **d)**Photographs of the thin section (sample 40), photo horizontal dimension is 6.5 mm.

Figure 11. Results of PSD (Particle Size Distribution) analysis (see appendix A2) for samples of Breccia II at the micro- and meso-scale (see Figure 10).*Left panels:* log-log plots of N(r) vs. r (mm) (PSD analysis). The trade-off length (r_k) marks the change of the slope of the lines. *Right panels:* log-log plots of the particles geometry dimensionanalysis (roughness fractal dimension) using the counting box method; the slope of the line is the fractal exponent.**a)** Sample 39 (micro-scale, thin section); **b)** Sample 40 (micro-scale, thin section); **c)** Sample 407 (meso-scale, on outcrop photograph); **d)** Sample 398 (meso-scale, on outcrop photograph).

Figure 12. Results of PSD analysis (D_r and D_s as in Table 3) plotted in the diagram we used to study the genesis of Breccia II (diagram after Jébrack, 1997); mesoscale samples (black dots labelled 398 and 407) fall at the boundary between "corrosive wear" and "volume expansion", whereas micro scale samples (black dots labelled 39 and 40) fall into the "volume expansion" field.

Figure 13. Dilation and slip tendency analysis (see appendix A4) for faults in Topinetti section (Figure 3d). Black dots pole to fault stereonets (lower hemisphere) on dilation and slip tendency using principal stresses attitude and stress ratio from sulfide, hematite and breccia II veins (Table 1).

Figure 14. Differential stress ($\Delta\sigma$) vs. pore fluid factor (λ_v) plot(see Appendix A3). We use the values of principal stresses derived by using Leslie and Sivrastava (2004) method (Table

5). The following values for the quartzite host rock have been used: density (ρ) 2700 kgm^{-3}, Poisson ratio (ν) 0.1-03, tensile strength (T) 10-30 MPa, cohesive strength (C): 1-10 MPa, and coefficient of internal friction (μ): 0.75. *Open diamond*: extension veins; *Open square*: hybrid veins (extensional shear); *Black cross*: low angle normal fault (non optimal oriented fault) θ_r=60°; *Open triangle*: high angle normal fault (optimal oriented fault) θ_r=30°. Extension failure mode, $\sigma_1-\sigma_3 < 4T$ and $\lambda_v = (\sigma_3 + T)/\sigma_v$; Hybrid extensional shear failure mode, $4T < \sigma_1-\sigma_3 < 5.66T$ and $\lambda_v=\sigma_3/\sigma_v+[8T(\sigma_1-\sigma_3) - (\sigma_1-\sigma_3)^2]/16T\sigma_v$; Shear failure mode (normal faulting), $\sigma_1-\sigma_3 > 5.66T$ and $\lambda_v = 1/2\mu\sigma_v[2C+\mu(\sigma_1+\sigma_3) -\mu(\sigma_1-\sigma_3)\cos2\theta_r - (\sigma_1-\sigma_3)\sin2\theta_r]$. The grey field is the range of the values of (λ_v) in Table 5.

Figure 15. Conceptual model of the formation of the Topinetti ore bodies. Left panels are the sketches of lithologies and structures involved, black thick arrows indicate extension direction and the envisaged stress regime at the time of mineralization. Right: Schematic pressure-time plot of the fluid pressure evolution for each deformation event. **a)** Along an impermeable/permeable layer interface (represented by the contact between green-purple pelite and quartzite), sulfide rich fluids pervasively soaked the quartzite and quartzite breccia layers. This pervasive flow precipitated intergranular pyrite leading to reduction of the bulk rock permeability (gentle pore fluid decrease during mineral deposition). **b)** Further event of sulfide-rich fluid influx during faulting, formation of Breccia I and pyrite rich veins. Pore pressure drops after mechanical failure leading to fluid venting, veining and breccia formation. Multiple events of fluid ingress are expected. **c)** Iron-rich fluid ingress during faulting, formation of Breccia II, hematite- rich veins and ore bodies. Fluid pressure sudden drops occur after veining and breccia formation again with multiple, cyclic events (cycle) of fluid pressure build up and decrease by faulting.

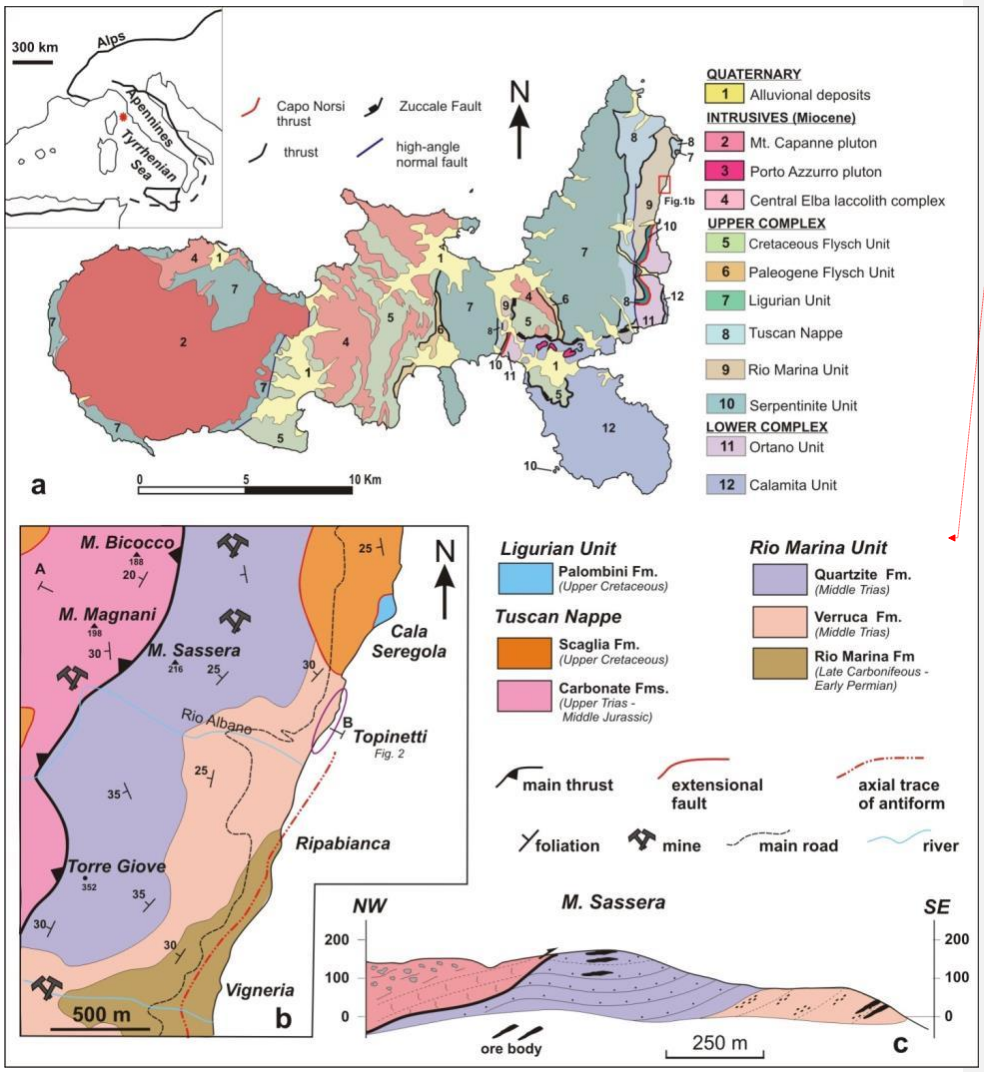

Figure 1

Formattato: Centrato

Formattato: Tipo di carattere: Non Grassetto

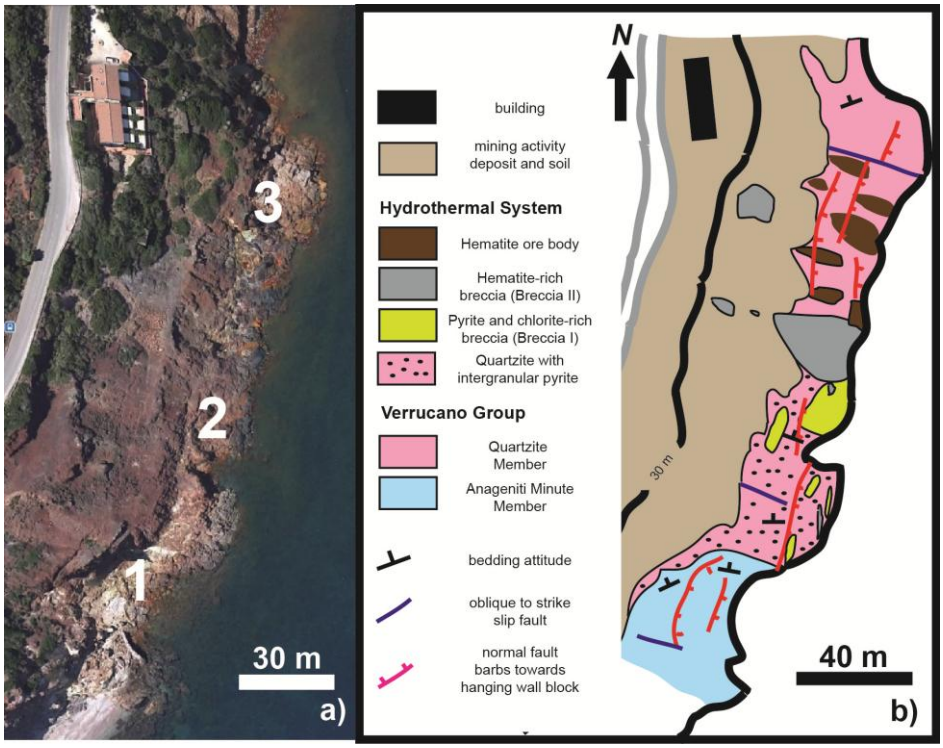

Figure 2

Formattato: Tipo di carattere: Non Grassetto

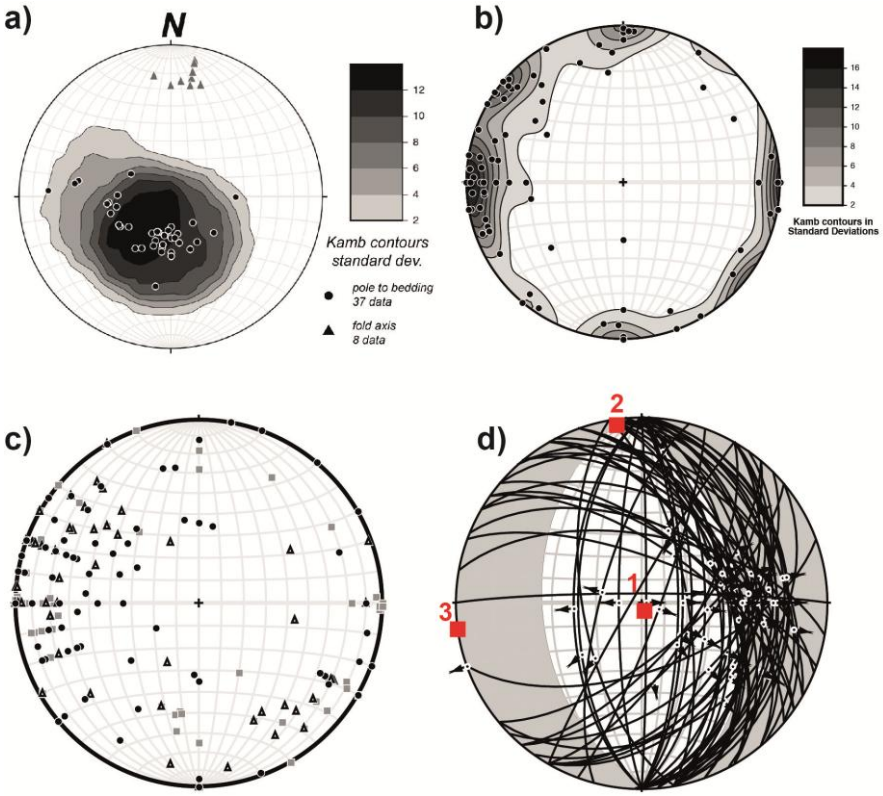

Figure 3

Formattato: Tipo di carattere: Non Grassetto

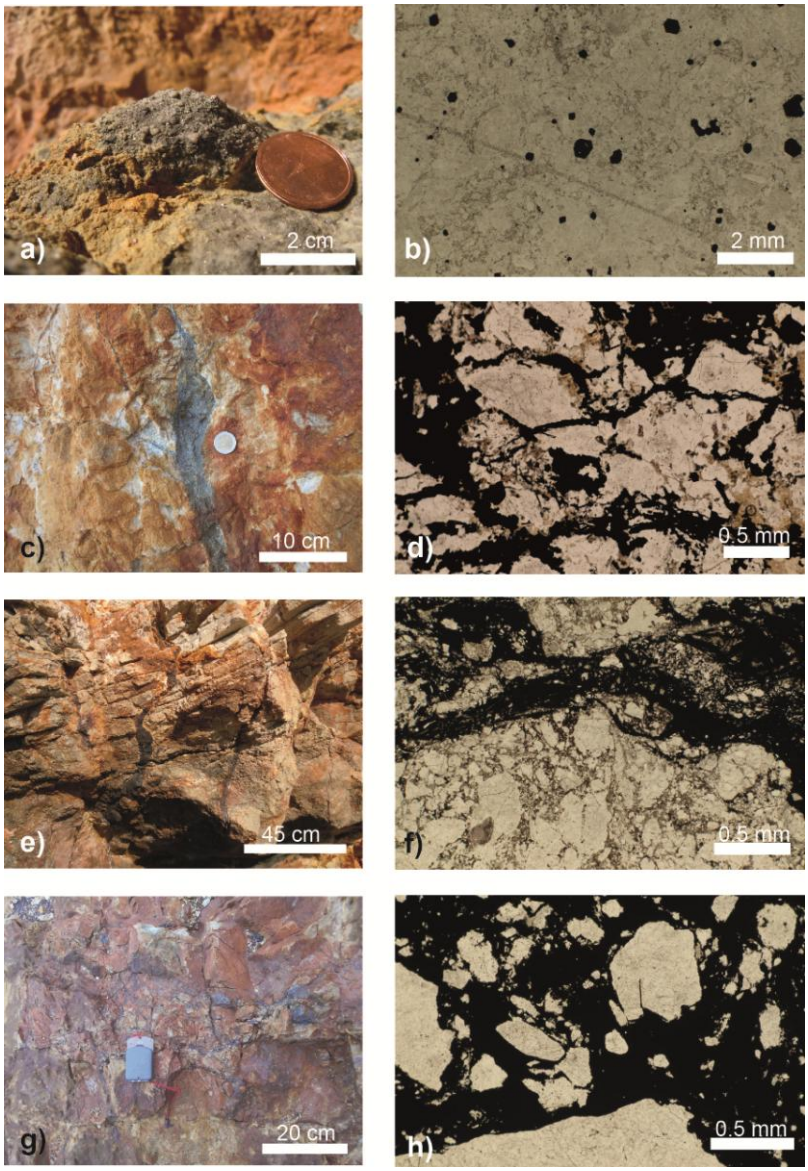

Figure 4

Formattato: Centrato

Formattato: Tipo di carattere: Non Grassetto

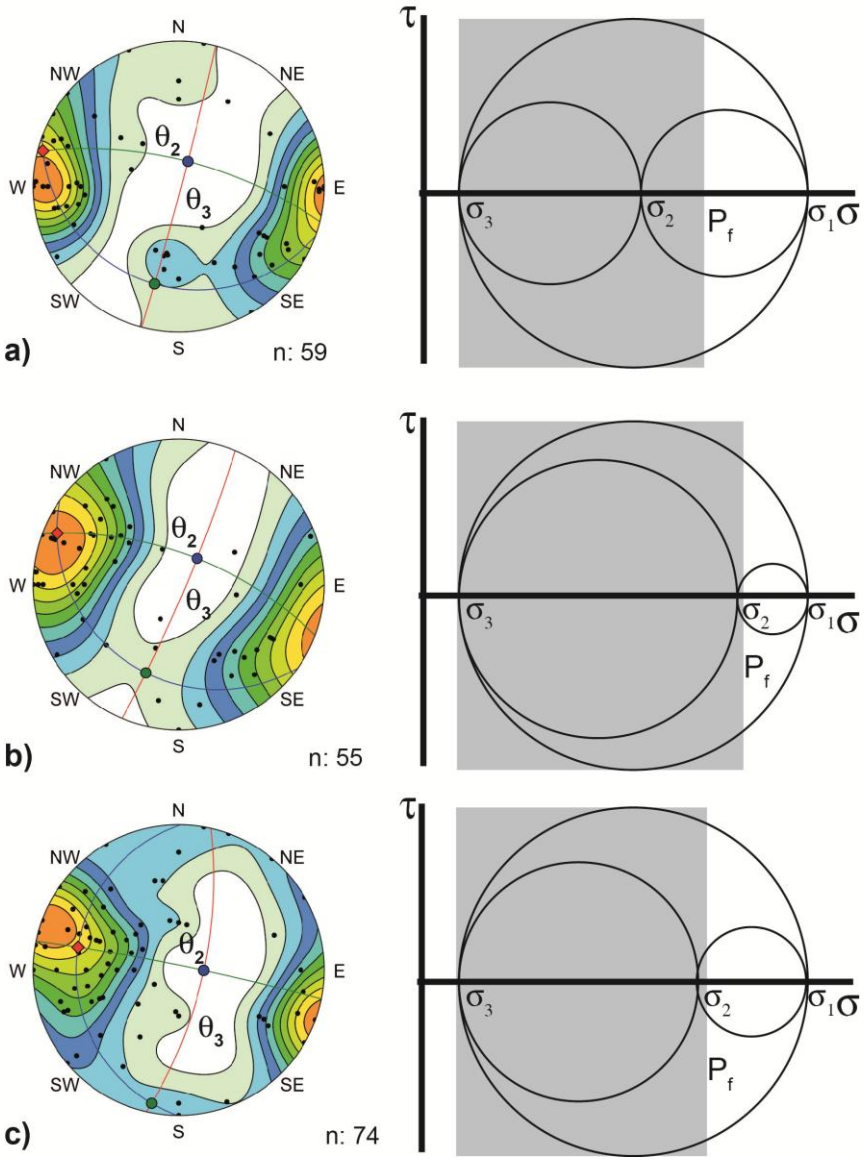

Figure 5

Formattato: Tipo di carattere: Non Grassetto

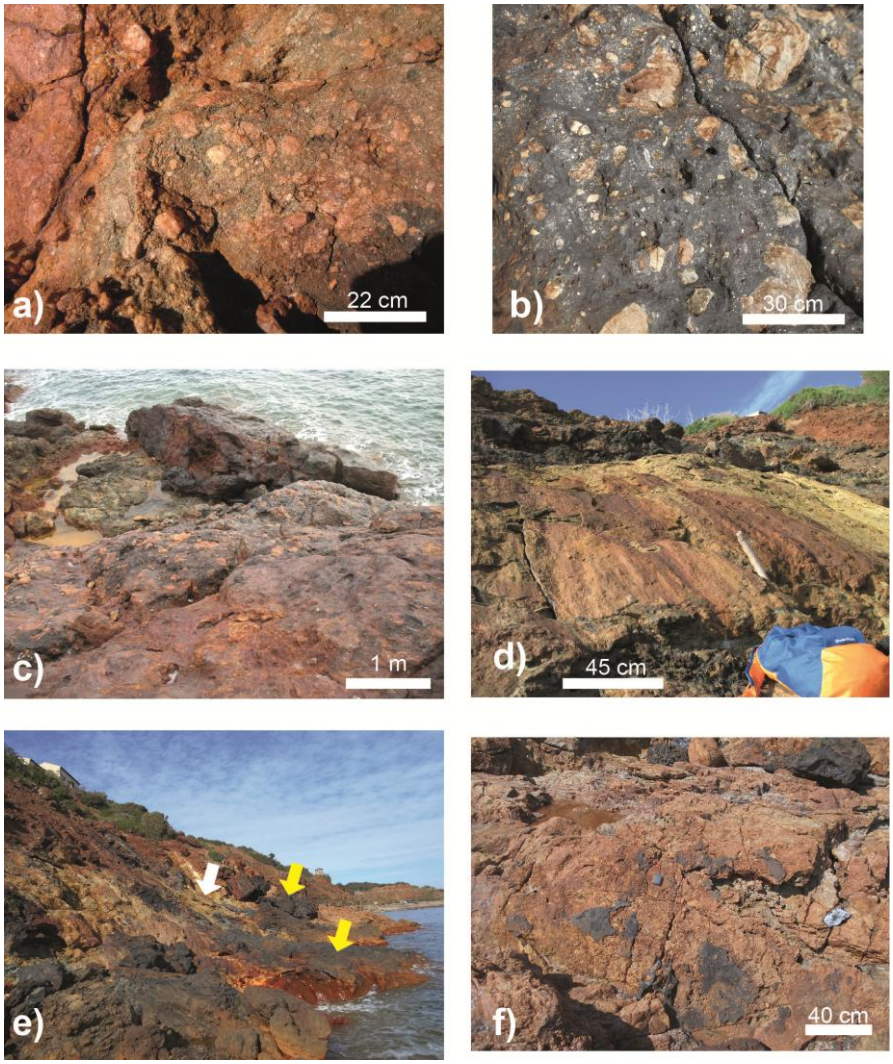

Figure 6

Formattato: Tipo di carattere: Non Grassetto

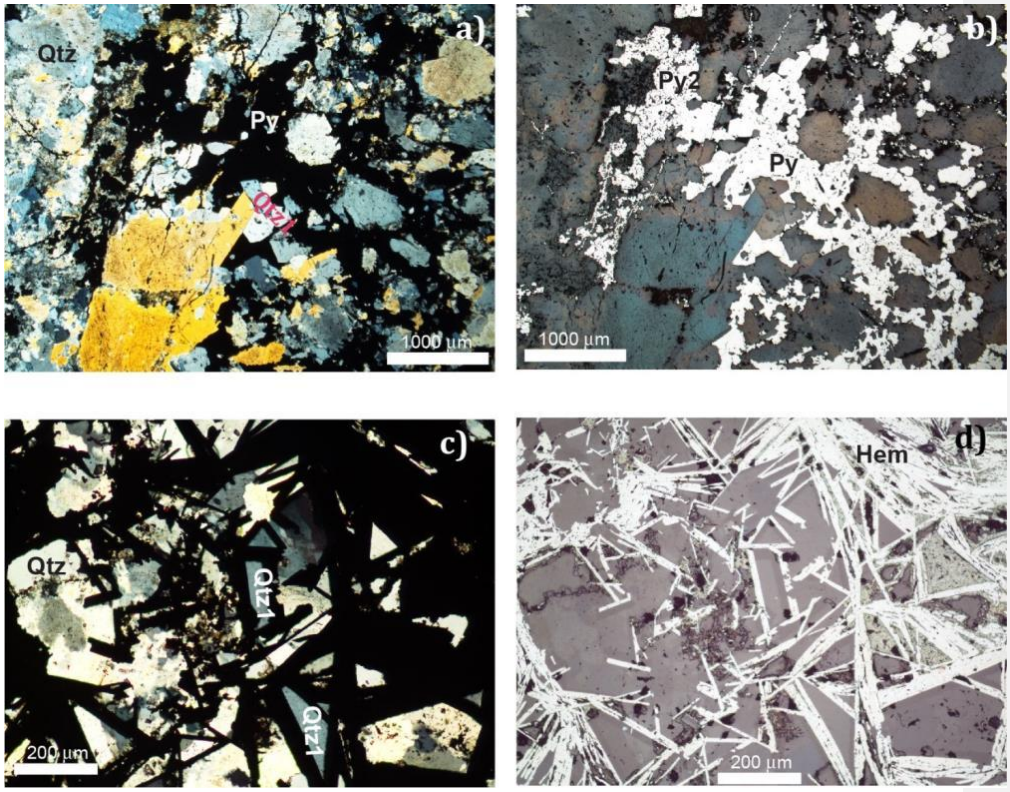

Figure 7

Formattato: Tipo di carattere: Non Grassetto

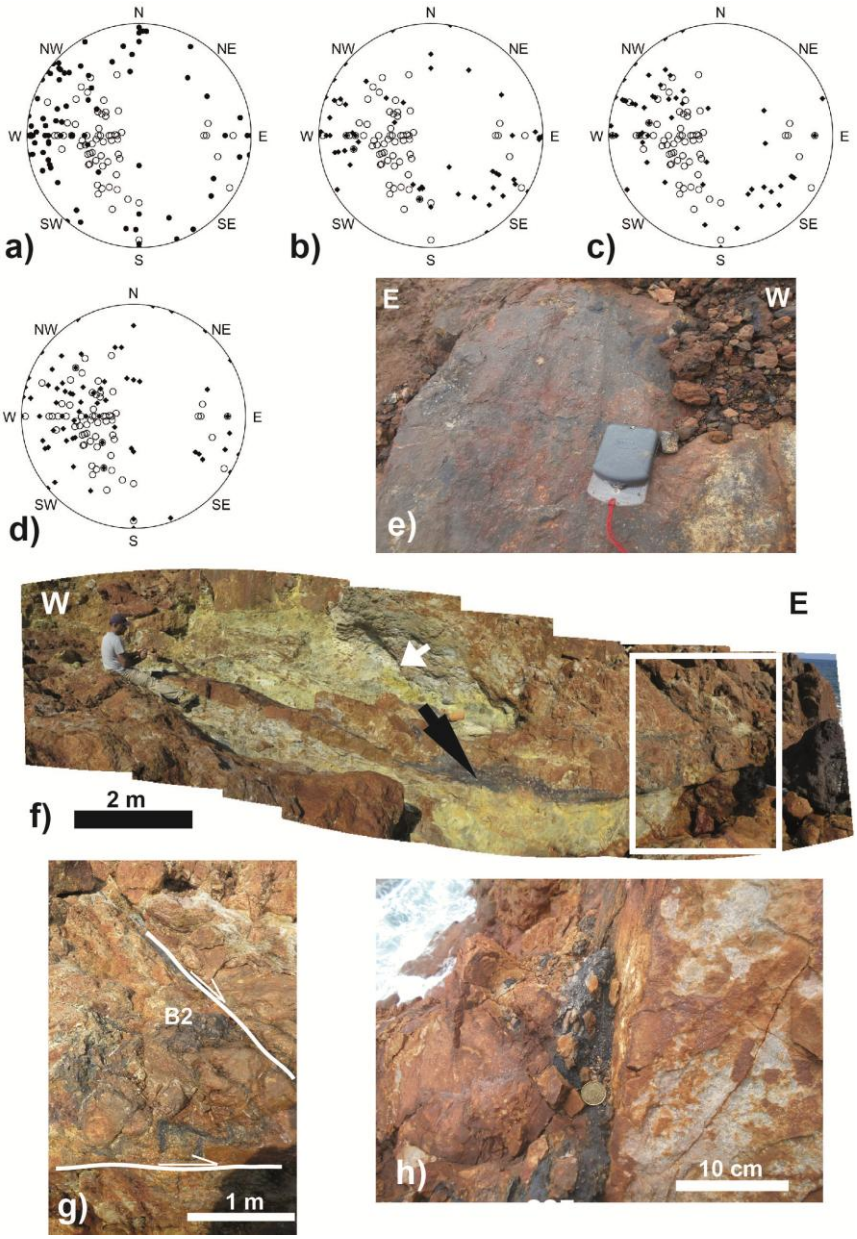

Figure 8

Formattato: Tipo di carattere: Non Grassetto

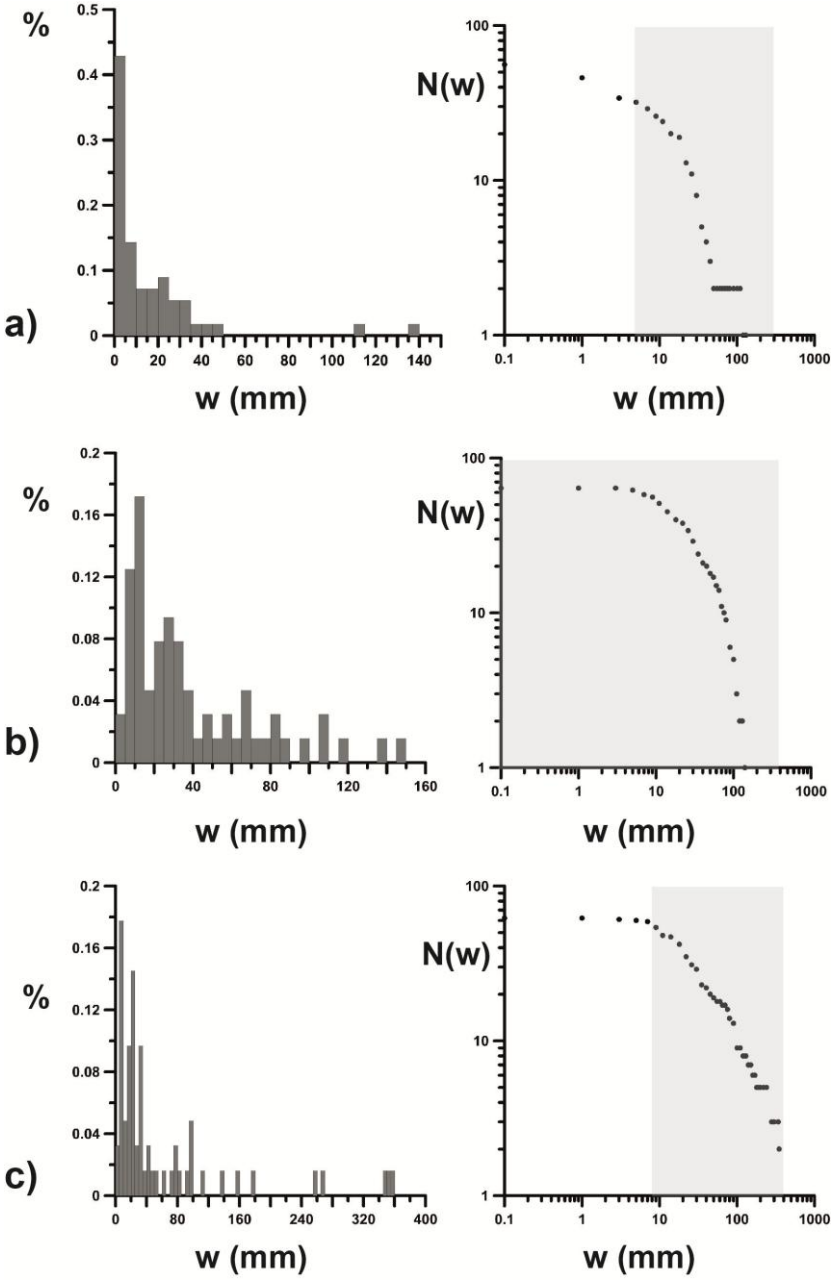

Figure 9

Formattato: Tipo di carattere: Non Grassetto

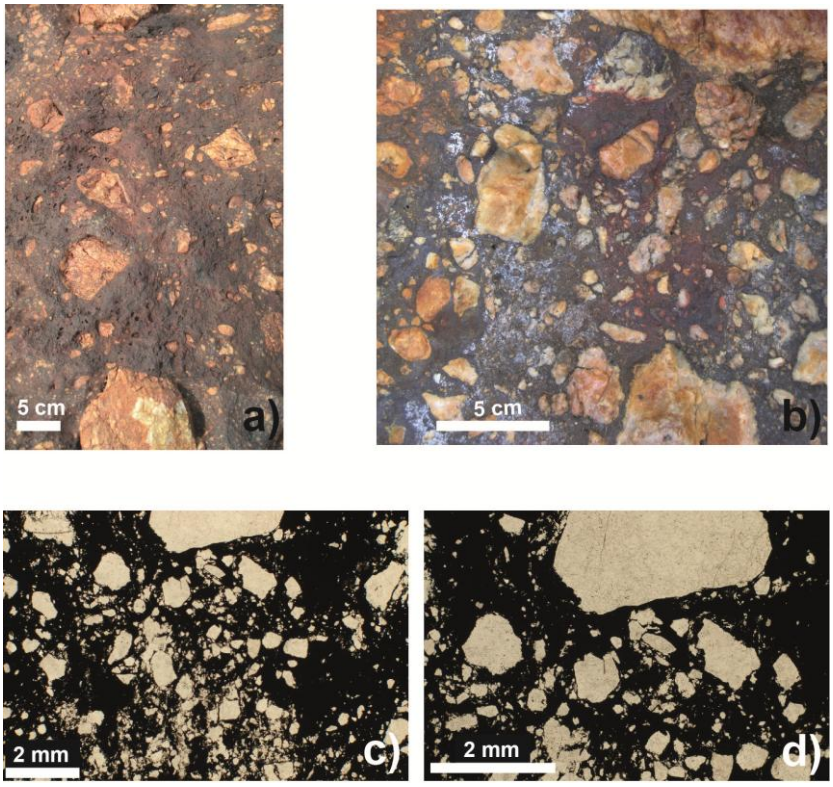

Figure 10

Formattato: Tipo di carattere: Non Grassetto

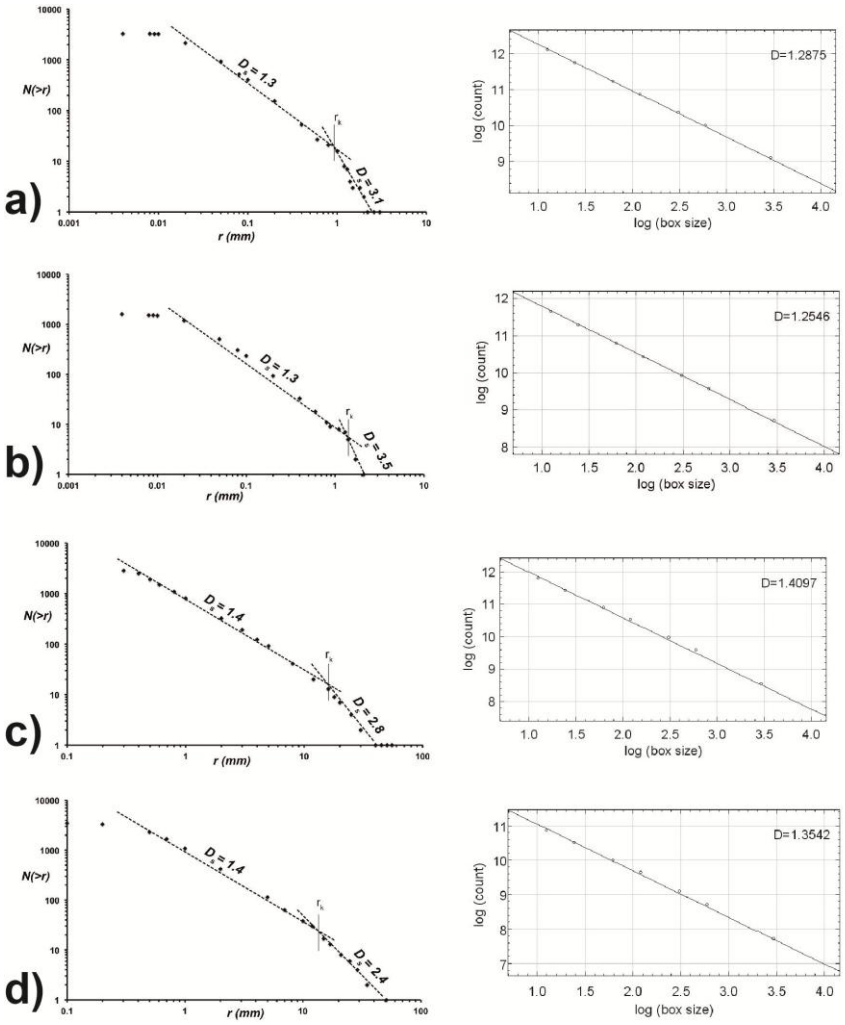

Figure 11

Formattato: Tipo di carattere: Non Grassetto

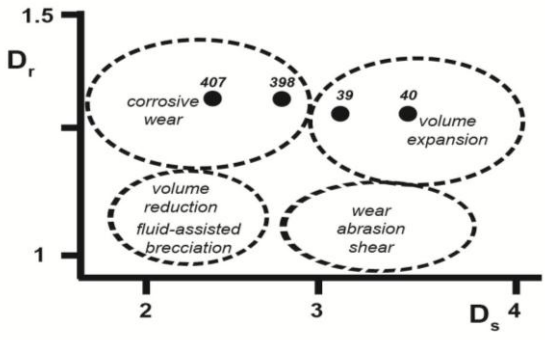

Figure 12

Formattato: Tipo di carattere: Non Grassetto

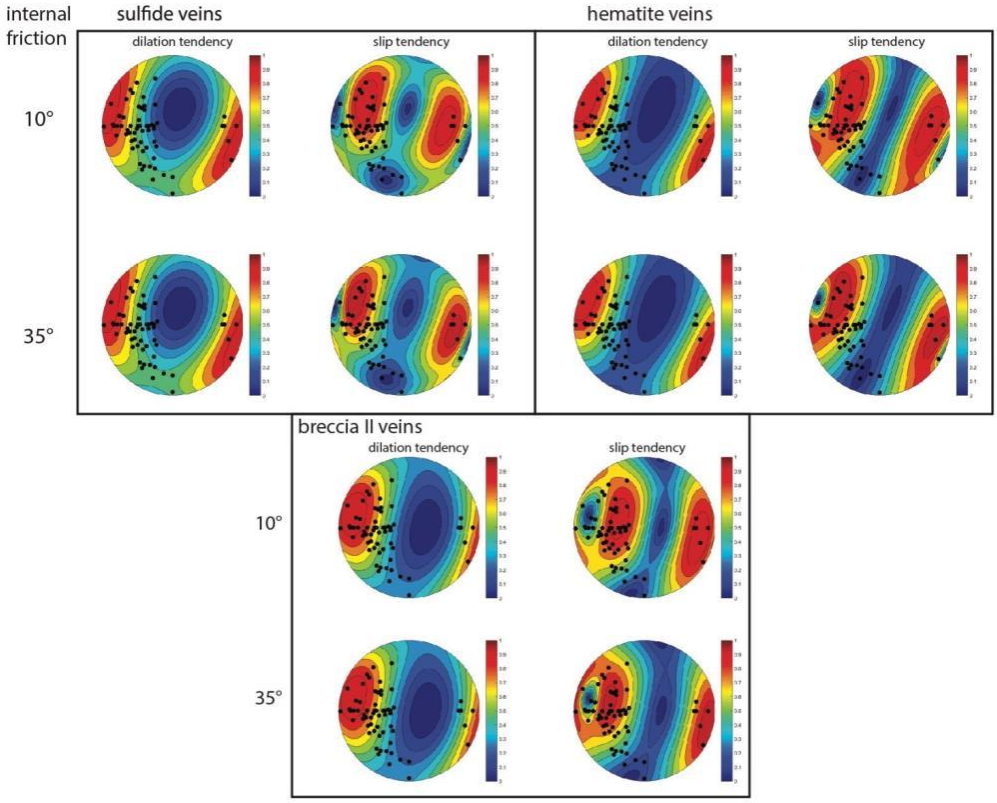

Figure 13

Formattato: Tipo di carattere: Non Grassetto

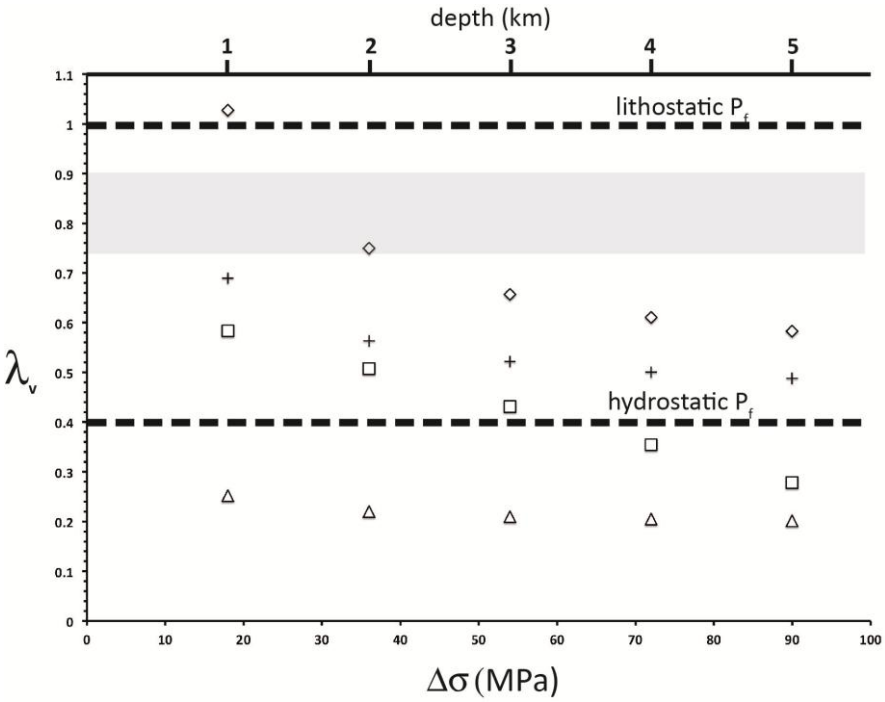

Figure 14

Formattato: Tipo di carattere: Non Grassetto

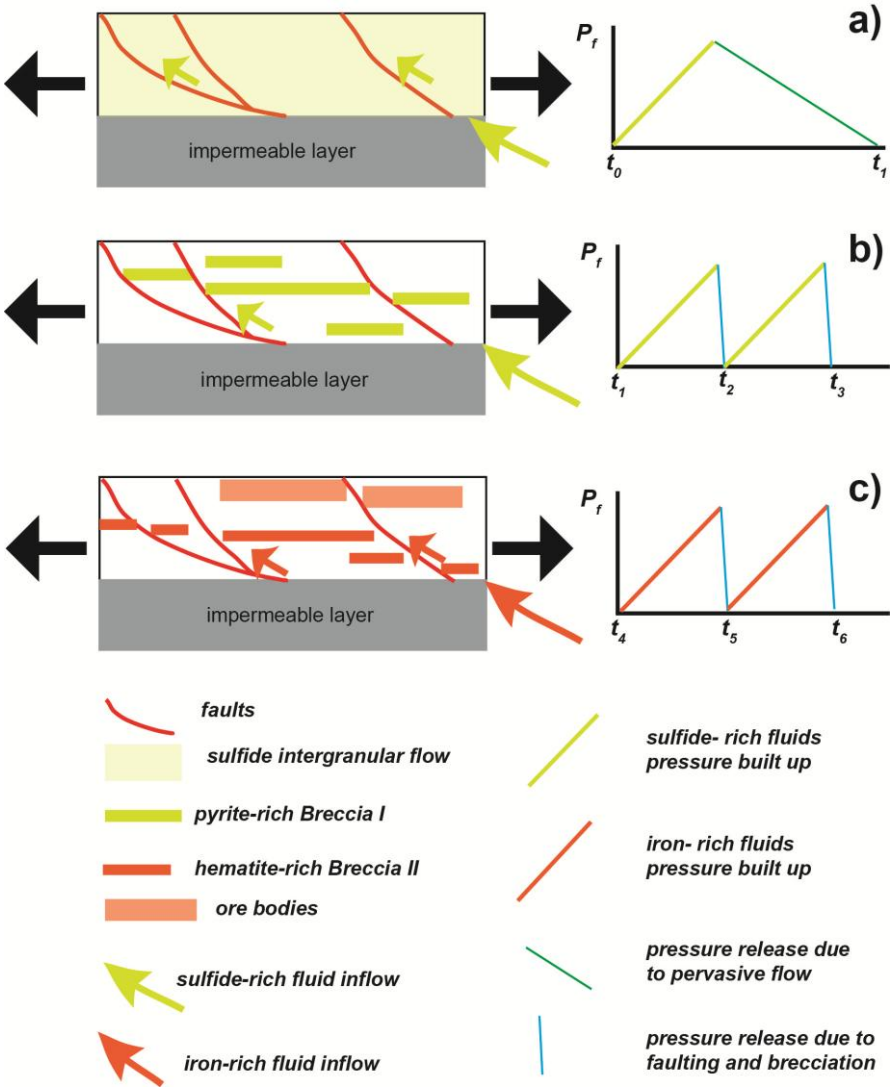

Figure 15

Formattato: Tipo di carattere: Non Grassetto